Structure and Stability of Carbohydrate–Lipid Interactions. Methylmannose Polysaccharide–Fatty Acid Complexes

Lan Liu,[1] Iwona Siuda,[2] Michele R. Richards,[1] Justin Renaud,[3] Elena N. Kitova,[1] Paul M. Mayer,[3] D. Peter Tieleman,[2] Todd L. Lowary[1] and John S. Klassen*[1]

Alberta Glycomics Centre and

[1]*Department of Chemistry, University of Alberta, Edmonton, Alberta, Canada T6G 2G2*

** E-mail: john.klassen@ualberta.ca*

[2]*Centre for Molecular Simulation Department of Biological Sciences, University of Calgary, Calgary, Alberta, Canada, T2N 1N4*

[3]*Chemistry Department, University of Ottawa Ottawa, Ontario, Canada K1N 6N5*

Keywords

Carbohydrates, lipids, mass spectrometry, molecular dynamics, NMR spectroscopy

Abstract

We report a detailed study of the structure and stability of carbohydrate–lipid interactions. Complexes of a methylmannose polysaccharide (MMP) derivative and fatty acids (FAs) served as model systems. The dependence of solution affinities and gas-phase dissociation activation energies (E_a) on FA length indicates a dominant role of carbohydrate–lipid interactions in stabilizing (MMP + FA) complexes. Solution ^{1}H NMR results reveal weak interactions between MMP methyl groups and FA acyl chain; MD simulations suggest the complexes are disordered. The contribution of FA methylene groups to the E_a is similar to that of heats of transfer of *n*-alkanes from the gas phase to polar solvents, suggesting MMP binds lipids through dipole–induced dipole interactions. MD results point to hydrophobic interactions and H-bonds with the FA carboxyl group. Comparison of collision cross sections of deprotonated (MMP + FA) ions with MD structures suggests that the gaseous complexes are disordered.

Introduction

Carbohydrates are essential biomolecules. They exist as free molecules in solution, as well as components of glycoproteins and glycolipids on the surfaces of cells.[1] These species play significant roles in varied molecular recognition events, including fertilization, inflammation, signal transduction, cell–cell adhesion and microbial infections.[2-4] In many cases, the biological activities of carbohydrates are mediated by protein recognition.[5] Carbohydrate–carbohydrate[4-6] and carbohydrate–lipid[7-11] interactions are also important, although these types of interactions are far less well studied. For example, the disaccharides trehalose and sucrose can protect lipid bilayers from dehydration and extreme temperatures,[7,8] but the underlying molecular interactions for these protective effects are not entirely clear.[10-12] Experimental and computational methods indicate that the main interactions are hydrogen bonds between the carbohydrates and the polar head groups of the lipids.[9-14] However, there is also evidence that the hydrophobic effect or other non-covalent interactions are involved.[15-17] Oligosaccharide and polysaccharide binding to hydrophobic ligands is also critically important to the delivery,[18-19] separation,[20-21] and stability[22-23] of bioactive molecules.

Although carbohydrates are overall hydrophilic due to the presence of many hydroxyl groups, the faces of many pyranose rings are hydrophobic,[24] and these can form specific inclusion complexes with fatty acids and other hydrophobic molecules.[21, 25-27] One well-known example is amylose, a polysaccharide of α-(1→4)-linked glucopyranose (Glc*p*) residues, residues; this adopts a helical structure when comprising at least 18 residues.[28] The interior of the helix is hydrophobic and the cavity can accommodate saturated and unsaturated fatty acids (FAs).[22, 27-28] Other polysaccharides can also form high affinity lipid complexes, for example the polymethylated polysaccharides (PMPs) produced by some mycobacteria.[29] There are two

classes of PMPs and they are suggested to play roles in regulating lipid metabolism.[29-30] One type consists of α-(1→4)-linked 6-*O*-methyl-Glcp residues (the same anomeric linkages as amylose) and are assumed to be helical.[31] The other type are 3-*O*-methylmannose polysaccharides (MMPs), which contain α-(1→4)-linked mannopyranose (Man*p*) moieties.[31-32] In MMPs, every Man*p* residue (except the non-reducing end) is methylated on O-3. Both types of PMPs bind to FAs and can enhance the activity of mycobacterial FA synthase.[33-34] Specifically, MMPs bind to long-chain linear fatty acids with affinities of 10^4–10^5 M^{-1}.[20, 35] Naturally occurring MMPs are produced with 10–13 Man*p* residues, with the most prevalent species containing 12 carbohydrate moieties.[20] It had been proposed that, , MMPs adopt a helical structure in the presence of lipids, with the methyl groups on the inside of the helix, thus creating a hydrophobic channel similar to the one found in amylose and cyclodextrins.[31-32] This structural hypothesis is based solely on similarities in the ^{1}H NMR chemical shifts between cyclodextrin and the (MMP + palmitic acid) complex.[36]

Given the structural similarities between starch/cyclodextrins and MMPs (α-(1→4)-linkages, similar stereochemistry at all but one stereogenic center) such a hypothesis seems plausible. However, naturally occurring MMPs are approximately half the length of that required for helix formation by starch fragments.[28] Furthermore, in complexes of starch bound to lipids,[37] the C3-hydroxyl group, which is methylated in MMPs, is located on the outside of the helix. The adoption of a helix with the methyl groups inside (referred to below as a "methyl-inside-helix") by MMPs would, in effect, require an "inversion" of the helix. In light of these data, we consider other structural models more plausible.

Given the importance of carbohydrate binding to lipids and hydrophobic molecules, there is a need to better understand the nature of these interactions.[38] Although several studies have

explored the nature of amylose–FA binding,[38-43] these have, by necessity, been limited to the solid phase since amylose is insoluble in water.[26] Unlike amylose, MMPs are highly soluble in water, providing a tractable system for studying carbohydrate–lipid interactions in aqueous solution. Moreover, we recently showed ESI-MS that (MMP + FA) complexes can be transferred intact from aqueous solution to the gas phase.[20] The ability to produce desolvated (MMP + FA) complexes provides an unprecedented opportunity to interrogate the nature of carbohydrate–lipid interactions free from solvent, thereby providing insight into the intrinsic energetics of these two classes of biomolecules.

Here we carried out the first investigation of the structure and stability of (MMP + FA) complexes in both aqueous solution and the gas phase. Association constants (K_a) were determined by ESI-MS, and NMR spectroscopy was used to probe the nature of the intermolecular interactions in aqueous solution. We used a synthetic MMP containing 14 Man*p* residues ("MMP", Scheme 1) that has an azidooctyl group on the reducing end. Its complexes with a series of saturated and unsaturated FAs (lauric acid (LA), myristic acid (MA), palmitic acid (PA), stearic acid (SA), oleic acid (SA-1), linoleic acid (SA-2) and linolenic acid (SA-3); Scheme 1) served as model systems in this study. Collision cross sections (CCS) derived from ion mobility separation (IMS)-MS measurements, thermal dissociation rate constants, and deuterium kinetic isotope effects, measured for the doubly deprotonated gas-phase ions of the (MMP + FA) complexes yield insight into their structures. Moreover, the dissociation activation energies (E_a) provide the first quantitative measure of the intrinsic energetics of carbohydrate–lipid interactions in the absence of solvent. The experimental measurements were supported with molecular dynamics (MD) simulations aimed at elucidating structural features of (MMP + FA) complexes in aqueous solution and in the gas phase.

Results and Discussion

Structure and stability of MMP and (MMP + FA) complexes in aqueous solution

Previous experimental studies of the interactions between MMP and FAs in aqueous solution made use of the naturally occurring polysaccharides, which contain a methyl group at the reducing end of the glycan.[36] In order to assess the impact of the azidooctyl group modification on complex formation, the structure of MMP in the presence and absence of PA in aqueous solution at neutral pH was studied by ^{1}H NMR spectroscopy (Figures S1–S8, Tables S1 and S2 in the Supporting Information). Substantial changes in chemical shifts were observed for the resonances of the anomeric hydrogens and methyl groups in MMP when PA was added; this is indicative of conformational reorganization of the glycan in the presence of the lipid (Figure 1). The trends in the changes were consistent with those observed in a previous investigation carried out at 180 MHz with the natural glycan.[36] From this, we conclude that the methyl-to-azidooctyl substitution at the reducing end does not substantially alter the structure of the (MMP + PA) complex in neutral aqueous solution. Moreover, it had been hypothesized that MMP, similarly to amylose, could form a helical structure in solution,[36] with the B face of the pyranose rings[44] forming a hydrophobic channel inside the helix and the 3-*O*-methyl groups lining the channel. Also similar to amylose, the hydrophobic cavity could bind FAs.[45-46] This model was proposed based on the similarity of the anomeric chemical shifts to those of cyclodextrin.[36] A helical MMP structure should have a more hydrophilic exterior and more hydrophobic interior than amylose, based on a comparison of cyclodextrins and cyclomannins (cyclic oligosaccharides of α-(1→4)-linked mannopyranose).[47-48] To test this hypothesis, TROESY NMR measurements were performed on MMP and the (MMP + PA) complex in aqueous solution. If the (MMP + PA) complex were helical, NOE cross peaks between PA and the signals for H3 and H5 (3.5–3.9

ppm) are expected. Similar cross peaks are clear in NOE experiments between amylose and hydrophobic guest molecules.[49] However, no such cross peaks were observed for (MMP + PA); instead, weak NOE signals between the 3-*O*-methyl group region and PA were detected (Figures S4 and S8). These results suggest that the PA does not reside inside a helical MMP and does not interact with the hydrophobic faces of the Man*p* rings to an appreciable degree (on the NMR time scale).

The "proxy protein" ESI-MS assay was used to evaluate the K_a of the (MMP + FA) complexes in aqueous ammonium acetate solutions at pH 8.5 and 25 °C (Table 1).[20] Bovine β-lactoglobulin (Lg), which served as a proxy protein (P_{proxy}) for these measurements, has a large and flexible hydrophobic cavity that binds long-chain FAs in basic solution and forms complexes that are kinetically stable in the gas phase.[50] Inspection of the affinities measured for LA, MA, PA and SA reveals that the natural logarithm of K_a increases nearly linearly with acyl chain length (Figure S9). This observation points to the dominant role of FA methylene–sugar interactions in stabilizing the (MMP + FA) complexes in aqueous solution. That a similar trend is found for (Lg + FA) complexes, wherein the acyl chain is known to be completely buried in the hydrophobic protein cavity, provides further support for this conclusion.[31, 36] Curiously, unsaturation of SA (i.e., SA-1, SA-2 or SA-3, Scheme 1) has no significant influence on K_a for the (MMP + SA) complexes, suggesting that methine groups (–CH=) are energetically similar to methylene groups ($–CH_2–$) in terms of their interactions with MMP in solution. In the case of binding to Lg, unsaturation of SA led to modest increases in affinity (Table S3).

MD simulations in aqueous solution were performed to gain insight into the structural features of hydrated (MMP + FA). Because of the lack of a crystal structure for (MMP + FA) complexes, several helical conformations were evaluated as initial starting geometries, including

ones based on structure of amylose (PDB 1C58)[37] and on the current proposed structure, where all the 3-*O*-methyl groups into the interior of the helix (methyl-inside-helix structure).[36] The methyl-inside-helix was found to unfold immediately into disordered conformations in the MD simulations, and this resulted in unrealistic (boat, half-chair) carbohydrate ring conformations. The initial conformation (Figure 2) was lower in energy and aligns the 3-*O*-methyl groups along the outside of the helical axis. Additionally, for (MMP + FA) complexes, structures in which the carboxyl group of the FAs is oriented towards the reducing end of MMP (Figure 2) are much lower in energy than structures in which the carboxyl group is oriented in the opposite direction (data not shown). Consequently, only the former was tested in the MD simulations.

During the solution simulations, the neutral MMP (MMP^0) completely unfolded (Figure 3), whereas when in complex with an FA, it only partially unfolded and was more compact than that of MMP^0 (Figure 3, S10 and S11). The helical structure disappeared in every case, and the simulations produced a large number of complex structures. The FA acyl chains interacted with the hydrophobic faces of the carbohydrate rings (i.e., the glycosidic oxygen and the C–H groups). The hydrophilic hydroxyl and 3-*O*-methyl groups are solvent exposed, though some of the 3-*O*-methyl groups shield the FA acyl chain from water molecules. The simulation results are consistent with the NMR data, which show only weak NOE signals between the FA acyl chain and 3-O-methyl groups, and no signals involving the H3 and H5 of the mannopyranose rings. Taken together, the simulation and NMR spectroscopic data suggest that the long-held model for this type of interaction[36] is incorrect, and that more heterogeneous collection of carbohydrate–lipid complexes exists in solution. These species presumably equilibrate quickly on the NMR time-scale and hence do not appear as well-resolved species that provide sufficient NOE transfer. The radii of gyration (r_{gyr}) were calculated over the course of the simulations (Figures S12–S19),

and in general, the r_{gyr} for the $(MMP^0 + FA)^{1-}$ complexes are smaller than for MMP^0 alone, consistent with a more compact conformation.

Structure and stability of (MMP + FA) complexes in the gas phase

Thermal rate constants (k) for the dissociation of the deprotonated gas-phase ions of the (MMP + FA) complexes at the –2 charge state (the major charged state produced by ESI, Figure S20) were determined from time-resolved blackbody infrared radiative dissociation (BIRD) measurements.[51-52] At the reaction temperatures investigated (73 to 120 °C) the $(MMP + FA)^{2-}$ ions dissociated exclusively by the loss of neutral FA (Figure S21), according to eq 1:

$$(MMP + FA)^{2-} \rightarrow MMP^{2-} + FA \quad (1)$$

Natural log plots of the normalized abundance (Ab/Ab_o) of $(MMP + FA)^{2-}$ against reaction time for each FA investigated (Figure S22) exhibit linear behavior, consistent with the presence of a single reactant ion structure or multiple, kinetically similar structures (Arrhenius parameters E_a and A in Table 1; corresponding Arrhenius plots for loss of FA in Figure S23.) Inspection of the Arrhenius parameters for the saturated FAs reveals that the dissociation E_a increases with acyl chain length. For the longer FAs (MA, PA and SA) the increase is linear, with each methylene group contributing, on average, 0.86 ± 0.02 kcal mol^{-1} (Figure 4). The linear increase with chain length suggests that MMP presents a relatively homogeneous environment to the methylene groups of the FAs in the gas phase. Remarkably, this energetic contribution is similar to that reported for the dissociation of gaseous deprotonated $(Lg + FA)^{n-}$ ions (0.82 ± 0.04 kcal mol^{-1}).[53] On its own, this surprising finding suggests that the intrinsic energetics of carbohydrate–lipid interactions are similar to those for protein–lipid binding. However, further studies are needed to establish the generality of this finding. These values, which are also similar in magnitude to the

contribution of methylene groups to the heats of transfer of *n*-alkanes from the gas phase to polar solvents, such as acetone (0.88 kcal mol^{-1}) and dimethylformamide (0.89 kcal mol^{-1}),[54-55] suggest that solvation of the FAs by MMP is primarily through dipole–induced dipole interactions.[31-32]

The E_a value determined for LA deviates considerably from the linear trend found for the longer FAs, with the E_a (21.5 kcal mol^{-1}) being much lower than expected (~24.5 kcal mol^{-1}). This indicates that the structure of the $(MMP + LA)^{2-}$ ion is somewhat different, at least in terms of intermolecular contacts, than the other $(MMP + FA)^{2-}$ ions investigated. The measured CCS values provide qualitative support for this conclusion (vide infra). The introduction of one or more double bonds into SA (i.e., SA-1, SA-2 and SA-3) has little effect on E_a; this is qualitatively consistent with trend in measured K_a values, and suggests that methine groups are energetically similar to methylene groups in terms of their role in stabilizing the (MMP + FA) complexes, both in solution and in the gas phase. It is also worth noting that the absolute E_a values are larger than those reported for the corresponding $(Lg + FA)^{n-}$ ions.[56] This finding, together with the similarity in the energetic contribution of individual methylene groups determined for both the MMP and Lg complexes, suggests the participation of the carboxyl group in stabilizing the $(MMP + FA)^{2-}$ ions, through neutral or ionic H-bonds. In this regard, we note that the formation of H-bonds between the carboxylate and the reducing end of the MMP appears to be a key stabilizing interaction in the gas phase.

In order to further demonstrate the importance of the acyl chain in stabilizing the $(MMP + FA)^{2-}$ ions, BIRD measurements were performed on two deuterated analogs of PA: PA-D3 (deuteration of the C16 methyl group) and PA-D31 (fully deuterated acyl chain; kinetic data for $(MMP + PA)^{2-}$, $(MMP + PA\text{-}D3)^{2-}$ and $(MMP + PA\text{-}D31)^{2-}$ ions at 92 °C in Figure S24).

Notably, partial or complete deuteration of the acyl chain of PA resulted in a measurable inverse deuterium kinetic isotope effect (KIE, 0.91 ± 0.03 for D3 and 0.66 ± 0.02 for D31). The deuterium KIE, which is attributed to the differential change in the vibrational frequencies of the deuterated and non-deuterated complex resulting from cleavage of the MMP-FA interactions,[57] is consistent with the presence of lipid–carbohydrate interactions in the gaseous $(MMP + FA)^{2-}$ ions. Moreover, the results obtained for the PA-D3 complex indicate that the PA methyl group interacts with MMP, at least in the $(MMP + PA)^{2-}$ ion.

Dissociation kinetics were also measured for the partially deuterated $(MMP + PA)^{2-}$ ion, i.e., $(D\text{-}MMP + PA)^{2-}$, which was produced from D_2O (representative ESI mass spectrum obtained following incubation of MMP in D_2O for 30 min at 25 °C in Figure S25). Analysis of the mass spectrum reveals an increase of 6 Da in the molecular weight of MMP. Notably, the kinetic data for the loss of PA from the $(MMP + PA)^{2-}$ and $(D\text{-}MMP + PA)^{2-}$ ions at 117 °C are indistinguishable (Figure S26). The absence of a KIE excludes the possibility that the KIEs measured for the $(MMP + PA)^{2-}$ ions consisting of PA-D3 and PA-D31 reflect differences in the internal energy distributions of the deuterated and non-deuterated ions resulting from differences in radiative energy transfer or any mass discrimination effects resulting from differential trapping of the deuterated and non-deuterated $(MMP + PA)^{2-}$ ions.[56,58]

These kinetic data provide compelling evidence that the $(MMP + FA)^{2-}$ ions are stabilized, in part, by sugar–lipid interactions. Moreover, the similarity in the magnitude to the contribution of methylene groups to the E_a measured values and reported heats of transfer of *n*-alkanes suggest that dipole–induced dipole interactions play a dominant role.

With the goal of more fully elucidating the nature of the interactions, CCS values for the gaseous, deprotonated MMP^{2-}, FA^-, and $(MMP + FA)^{2-}$ ions were determined from IMS

measurements, and the results compared to CCS values calculated for structures obtained from MD simulations. A series of calibrants with known CCS values (in He) were used to establish CCS values from the IMS measurements (Table S4 and Figure S27). The measured CCS values for the saturated FA^- ions suggest that they increase (from 136 to 142 $Å^2$), as one would expect, with increasing chain length (Tables S5). The CCS values of the three unsaturated SAs (SA-1, SA-2, and SA-3) were somewhat smaller (~4%) than that of SA, presumably due to bending of lipid chain caused by the *cis* double bonds, and are similar to that of MA. The CCS values measured for the $(MMP + FA)^{2-}$ ions were somewhat larger than for the MMP^{2-} ion (414 $Å^2$), and increased with the size of the saturated FA (from 441 (LA) to 457 $Å^2$ (SA)). For the MMP complexes with the three unsaturated SAs, the CCS values are between those of the $(MMP + PA)^{2-}$ and $(MMP + SA)^{2-}$. The rather modest increase in CCS values upon FA binding is, on its own, consistent with MMP forming inclusion complexes with the FAs. Interestingly, a linear increase in CCS, from 440 to 457 $Å^2$, with acyl chain length is observed for MA, PA and SA; the CCS value for the $(MMP + LA)^{2-}$ ion was smaller than expected, based on this relationship (Figure 4). This trend is analogous to the trend in E_a.

CCS values were also calculated for structures generated from the gas-phase MD simulations and compared with the experimental values. The CCS values calculated for the initial, helical structures are 21–31% larger than the experimental CCS values (Figures S28–S35). The CCS values decrease after equilibration and are 4–16% larger than the experimental CCS values (Supporting Information). During simulations, the calculated CCS values varied; in most of the cases, they fall within or are close to the upper error ranges of the corresponding experimental CCS values.

Similarly to the solution simulations, the helix-like structure of the MMP^{2-} collapsed during the gas-phase simulations and led to a variety of structures. There was no specific arrangement of the Man*p* rings, and the hydroxyl groups are oriented outwards. The 3-*O*-methyl groups either point outwards or towards the collapsed structure. In all of the gas-phase simulations of $(MMP + FA)^{2-}$, the FA chain stayed in the proximity of MMP^{2-}. It was either wrapped with MMP^{2-} (although helix-like structure was lost), or it stayed on the surface of MMP^{2-}. In 90% of the simulations, the position of the FA chain is stabilized by a hydrogen bond between the -COOH group and O-1 atom of the first carbohydrate ring of MMP^{2-}. This hydrogen bond is formed in the first nanosecond of simulation and remained throughout the simulation. In the subsequent simulations, the hydrogen bond to O-1 was not formed or was lost to the one of the other hydroxyl groups of MMP^{2-}. Throughout the simulations, when FA stayed inside the MMP^{2-}, it interacts mostly with the hydrophobic patches on MMP^{2-} rings, similar to the initial structure of $(MMP + FA)^{2-}$ complexes.

Conclusions

We have described the first detailed study of the structure and stability of carbohydrate–lipid complexes in aqueous solution and in the gas phase. Although a number of such interactions are present in nature, we focused on complexes between mycobacterial MMPs and FAs. This study produced a number of significant findings. Firstly, data from solution NMR measurements cast doubt on the long-held structural model used to explain MMP–lipid interactions in aqueous solution, where MMP adopts a helical structure with the methyl groups thereby creating a hydrophobic channel inside the helix.[36] Secondly, the dependency of solution affinities and gas-phase dissociation E_a values on the length of the FA acyl chain shows conclusively that

carbohydrate–lipid interactions play a significant role in stabilizing (MMP + FA) complexes, both in their hydrated and dehydrated forms. Moreover, the gas-phase data provide the first quantitative measure of the intrinsic (in the absence of solvent) energetics of carbohydrate-lipid binding. Finally, molecular modeling indicated that, in solution, MMP is not a single, helical conformation; rather, it adopts a number of rapidly equilibrating, kinetically similar structures, with the FA acyl chain interacting with the hydrophobic faces of the carbohydrate rings. Similarly, in the gaseous $(MMP + FA)^{2-}$ ions, MMP adopts a disordered structure and interacts with the FA acyl chains through the hydrophobic faces of the carbohydrate rings and H-bonds with the FA carboxyl group. Additional measurements (e.g. solid-state NMR spectroscopy[59-60] or X-ray crystallography) are needed to characterize fully the structures of the (MMP + FA) complexes. However, the dynamic equilibrium of complexes will greatly complicate efforts to gain additional structural insights through experimental methods.

Experimental Section

Samples and sample preparation

MMP (molecular weight (MW) 2623.6 Da) was synthesized and purified as described previously.[20] Lg (monomer 18281 Da), LA (200.3 Da), MA (228.4 Da), PA (256.4 Da), SA (284.8 Da), SA-1 (282.5 Da), SA-2 (280.4 Da), SA-3 (278.4 DaPA-D31 (287.6 Da) and insulin chain A (InsA, 2532.0 Da) were purchased from Sigma–Aldrich Canada (Oakville, Canada). PA-D3 (259.4 Da) was purchased from ACP Chemicals (St. Leonard, Canada). dT10 DNA (2979.6 Da) was purchased from Integrated DNA Technologies.

A stock solution of MMP was prepared in Milli-Q water. Stock solutions of FAs were prepared by in methanol. Lg was dissolved and exchanged directly into Milli-Q water in an Amicon

microconcentrator (MWCO 10 kDa), and stored at –20 °C. Lg concentration was determined by lyophilizing a known volume of the filtrate and measuring the mass of the protein. ESI solutions were prepared from the stock solutions in ammonium acetate (10 mM, pH 8.5 adjusted with ammonium hydroxide); imidazole (10 mM) was added to reduce dissociation.[50] Stock solutions of CCS calibrants InsA, dT10 DNA and PS,[61-]were prepared following the procedure outlined by Smith et al.[64]

NMR spectroscopy

NMR spectra of MMP and MMP with PA were acquired in D_2O at 27 °C on a VNMRS 700 MHz spectrometer (Aglient Technologies) equipped with a cold probe. (MMP+PA) was prepared according to the procedure described by Yabusaki et al,[36] and was at a similar concentration (MMP/PA ≈1:2, based on the integration of the ^{1}H NMR spectrum). The spectra were referenced to an external standard of acetone (2.22 ppm for 1H), and 1D 1H, gCOSY, gTOCSY, and TROESY[65] spectra were obtained. For all spectra, the intensity of the residual HOD peak was decreased by using a pre-saturation pulse sequence, irradiating at 4.76 ppm. 1D ^{1}H spectra were acquired in 512 transients with a spectral window of 8389 Hz (10.76 to –1.22 ppm). Line broadening was applied in the Fourier transformations to improve signal-to-noise (0.5 Hz for MMP; 1.0 Hz for MMP with PA). The 2D spectra were acquired with 64 transients in F2, 450 increments in F1, and a spectral window of 4195 Hz (6 to 0 ppm). A mixing time of 0.1 s was used for the gTOCSY, and a mixing time of 0.4 s was used for the TROESY. For all 2D spectra, sine-bell functions were applied interactively to improve signal-to-noise, but no line-broadening was used.

Molecular dynamics (MD) simulations

Two species of MMP were generated (described above): doubly deprotonated gaseous MMP (MMP^{2-}), with negative charges assigned to the oxygen O2 of the 2nd and 14th Man*p* residues in order to reduce Coulombic repulsion; and neutral, solution MMP (MMP^{0}, Figure 2). In order to establish the helical conformation, the Φ dihedral angle (O5–C1–O4–C4) was set to 100° and the Ψ dihedral angle (C1–O4–C4–C5) was set to –85° for each carbohydrate residue. The azidooctyl synthetic tag was attached to 14th residue (the reducing end). Both MMP^{2-} and MMP^{0} were simulated on their own and as a 1:1 complex with LA, MA, PA, SA, SA-1, SA-2 or SA-3. The acyl chain of each neutral FA was placed inside MMP^{2-} with the FA carboxylic acid pointing towards the azidooctyl tag, forming an $(MMP^{2-} + FA)^{2-}$ complex (Figure 2). Similarly, the acyl chain of each deprotonated FA was placed inside MMP^{0}, with the FA carboxylate group pointing towards the azidooctyl tag, giving a $(MMP^{0} + FA)^{1-}$ complex. According to molecular modelling, structures in which the carboxyl group of the FAs is oriented towards the reducing end of MMP are much lower in energy than when the carboxyl group is oriented in the opposite direction (data not shown). Consequently, only this orientation was considered for the MD simulations.

The system was set up using xLeap program (AMBER12 package).[66-67] The GLYCAM_06h force field[68] was used for the polysaccharide part of the MMP and the generalized AMBER force field (GAFF, version 1.5)[69] for the FA chains and the azidooctyl group. Charges for the FA chains and azidooctyl group were assigned using the AM1 with Bond Charge Correction (AM1-BCC) model within the Antechamber program (AmberTools13).[66-67] For each system, three independent simulations were run.

For the gas-phase simulations, both MMP^{2-} and $(MMP^{2-} + FA)^{2-}$ were minimized, heated to 300 K during 15 ps run with 0.5 fs time step, and equilibrated for 10 ps (0.5 fs time step) at 300 K. Each system was run for 100 ns (0.5 fs time step). For the simulations in aqueous solution, MMP^{0} and $(MMP^{0} + FA)^{1-}$ were placed in a truncated octahedron box and solvated with a 25 Å pad of TIP3P water molecules.[70] One sodium ion was added to neutralize the system. During initial minimization, the structures of MMP^{0} and $(MMP^{0} + FA)^{1-}$ were constrained using strong restraints (500 kcal mol–1 $Å^{-2}$) to allow the water molecules and ion to relax around MMP^{0} or $(MMP^{0} + FA)^{1-}$. The restraints were then released and the entire system was minimized. Next, each system was heated to 300 K during a 20 ps run (2 fs time step) at constant volume (NVT) with weak restraints (10 kcal mol–1 $Å^{-2}$) on MMP^{0} or $(MMP^{0} + FA)^{1-}$. The Langevin thermostat[71] was used with a collision frequency of 1.0 ps^{-1}. A 9.0 Å cutoff was used for non-bonded interactions and the Particle Mesh Ewald method[72] was used for calculation of long-range electrostatics. Equilibration was run for 10 ps (2 fs time step) in the NPT ensemble using isotropic pressure scaling and a relaxation time of 2 ps. Each system was run for 40 ns simulation time (2 fs time step).

The simulation analysis considered 100 ns of each of the gaseous simulations of MMP^{2-} and $(MMP^{2-} + FA)^{2-}$, and 40 ns of each of solution simulations of MMP^{0} and $(MMP^{0} + FA)^{1-}$. The theoretical CCS was calculated every 10 ps for each gaseous simulation, in quadruplicate, using the MOBCAL program[73-74] with the trajectory method. Before submitting MMP^{2-} and $(MMP^{2-} + FA)^{2-}$ structures for the CCS calculations, each structure was cooled to 0 K during 15 ps run (0.5 fs time step) for simulation and then minimized. For all the solution simulations, the radius of gyration (r_{gyr}) was calculated to describe the spatial arrangement of MMP^{0} and FA^{1-} with respect

to each other. These values were calculated a using TCL script (VMD program).[75] Mass weighted r_{gyr} was calculated separately for MMP, FA chain, and (MMP + FA).

Mass spectrometry

The affinities of the (MMP + FA) complexes (1:1) in aqueous solution were measured with a proxy protein ESI-MS assay,[20] and the gas-phase dissociation rate constants were measured with BIRD.[51-52] Both sets of measurements were performed on a 9.4 tesla ApexII FTICR mass spectrometer (Bruker) equipped with a nanoflow ESI ion source. Nanoflow ESI was performed using borosilicate tubes (1.0 mm o.d., 0.68 mm i.d.) pulled to ~5 μm o.d. at one end using a P-2000 micropipette puller (Sutter Instruments, Novato, CA). A platinum wire was inserted into the nanoESI tip and –1 kV was applied. Details of the instrumental and experimental conditions for BIRD measurements are elsewhere.[53]

Experimental CCS values were determined using a Synapt G2-S quadrupole-ion mobility separation-TOF (Q-IMS-TOF) mass spectrometer (Waters, Milford, MA). ESI was carried out using nanoESI (capillary voltage –1.3 kV, cone voltage of 35 V, source block temperature 60 °C, trap energy < 3 V, transfer energy 2 V). Argon was used in the trap and transfer ion guides (2.33×10^{-2} mbar and 2.47×10^{-2} mbar, respectively). The flow rate of helium into the chamber directly preceding the traveling wave ion mobility separation (TWIMS) device was 180 mL min^{-1}. All traveling-wave IMS measurements were carried out using N_2 as the mobility gas (flow rate of 90 mL min^{-1}). The wave pulse height was set to 35 V; the wave velocity was 800 m s^{-1}. Data acquisition and processing was carried out using MassLynx (v 4.1, Waters).

ESI-MS binding measurements

A proxy protein ESI-MS assay was used to quantify K_a for the (MMP + FA) complexes.[20] Lg, which is known to bind to long-chain FAs in basic solution and forms kinetically-stable gaseous complex ions,[50] served as the proxy protein. The assay and procedures for data analysis are reported elsewhere.[20]

BIRD kinetic data

The dissociation rate constant (k) for the loss of neutral FA from the gas-phase $(MMP + FA)^{2-}$ ion, at a given temperature, was determined from a linear least-squares fit of the plot of the natural logarithm of the normalized abundance (Ab/Ab_0) of the reactant ion versus reaction time (eq 2):

$$\ln Ab/Ab_0 = -kt \quad (2)$$

The value of Ab/Ab_0 was calculated using eq 3:

$$Ab/Ab_0 = Ab_{(MMP+FA)} / (Ab_{(MMP+FA)} + Ab_{MMP}) \quad (3)$$

where $Ab_{(MMP+FA)}$ and Ab_{MMP} are the abundances measured for the deprotonated $(MMP + FA)^{2-}$ reactant ion and the $(MMP)^{2-}$ product ion, respectively.

Collision cross sections (CCS) measurements

Determination of CCS from drift time measurements used protocol described elsewhere.[76-77] Briefly, the IMS drift (arrival) times of ions of InsA,[61] dT10 DNA,[62] and PS,[63] which have known CCS (in He), were analyzed under the same experimental conditions as the $(MMP + FA)^{2-}$ and $(MMP)^{2-}$ ions to establish a correlation between the measured drift times (t_D) and CCS. The t_D values were corrected for both mass-dependent and mass-independent flight times using eq 4:

$$t_D' = t_D - \frac{c\sqrt{\frac{m}{z}}}{1000} \quad (4)$$

where t_D' is the corrected drift time (in ms) and t_D is the measured drift time (in ms); the enhanced duty cycle delay coefficient (c) was determined wtih Synapt G2-S software.[76] The reported CCS values (in He) for the calibrant ions were corrected for charge and reduced mass (μ) using eq 5:

$$\text{CCS}' = \frac{\text{CCS}\sqrt{\mu}}{z} \quad (5)$$

where CCS' is the corrected collision cross section in He (t_D' and CCS' for each calibrant ion in Table S4). The plot of ln(CCS') versus ln(t_D') is linear (Figure S27a): the slope (0.634) corresponds to the exponential factor, X, an empirical parameter.[78] Using the empirically-determined value of X, the final, corrected drift times (t_D'') were calculated from eq 6:

$$t_D'' = (t_D')^X (z/\sqrt{\mu}) \quad (6)$$

The plot of literature CCS values versus t_D'' is also linear, with R^2 = 0.998 (Figure S27b. The CCS values of the deprotonated MMP^{2-} and $(MMP + FA)^{2-}$ ions were determined from the calibration curve and the corresponding t_D'' values.

Acknowledgements

The authors are grateful for financial support provided by the Natural Sciences and Engineering Research Council of Canada and the Alberta Glycomics Centre.

References

[1] A. Varki, N. Sharon, in Essentials of Glycobiology, 2nd ed. (Eds.: A. Varki, R. D. Cummings, J. D. Esko, H. H. Freeze, P. Stanley, C. R. Bertozzi, G. W. Hart, M. E. Etzler.), Cold Spring Harbor Laboratory Press, Cold Spring Harbor (NY), **2009**.

[2] N. Sharon, H. Lis, *Sci. Am.* **1993**, 268, 82–89.

[3] F. A. Quiocho, *Ann. Rev. Biochem*. **1986**, 55, 287–315.

[4] I. Bucior, M. M. Burger, *Curr. Opin. Struc. Biol*. **2004**, 14, 631–637.

[5] H. Lis, N. Sharon, *Chem. Rev*. **1998**, 98, 637–674.

[6] B. Lorenz, L. Álvarez de Cienfuegos, M. Oelkers, E. Kriemen, C. Brand, M. Stephan, E. Sunnick, D. Yüksel, V. Kalsani, K. Kumar, D. B. Werz, A. Janshoff, *J. Am. Chem. Soc.* **2012**, 134, 3326–3329.

[7] J. H. Crowe, L. M. Crowe, J. F. Carpenter, C. Aurell Wistrom, *Biochem. J.* **1987**, 242, 1–10.

[8] J. H. Crowe, L. M. Crowe, J. F. Carpenter, A. S. Rudolph, C. A. Wistrom, B. J. Spargo, T. J. Anchordoguy, *Biochim. Biophys. Acta, Rev. Biomembranes* **1988**, 947, 367–384.

[9] G. van den Bogaart, N. Hermans, V. Krasnikov, A. H. de Vries, B. Poolman, *Biophys. J.* **2007**, 92, 1598–1605.

[10] H. D. Andersen, C. Wang, L. Arleth, G. H. Peters, P. Westh, *Proc. Natl. Acad. Sci. U.S.A.* **2011**, 108, 1874–1878.

[11] G. Moiset, C. A. López, R. Bartelds, L. Syga, E. Rijpkema, A. Cukkemane, M. Baldus, B. Poolman, S. J. Marrink, *J. Am. Chem. Soc*. **2014**, 136, 16167–16175.

[12] J. Kapla, J. Wohlert, B. Stevensson, O. Engstrom, G. Widmalm, A. Maliniak, *J. Phys. Chem. B*. **2013**, 117, 6667–6673.

[13] N. V. Ivanisenko, S. A. Dzuba, *Appl. Magn. Resn*. **2013**, 44, 883–891.

[14] J. Tian, A. Sethi, Basil I. Swanson, B. Goldstein, S. Gnanakaran, *Biophys. J.* **2013**, 104, 622–632.

[15] A. Choutko, W. F. van Gunsteren, P. H. Huenenberger, *ChemPhysChem* **2011**, 12, 3214–3223.

[16] B. Deme, T. Zemb, *Curr. Opin. Colloid Interface Sci*. **2011**, 16, 584–591.

[17] D. Wrobel, D. Appelhans, M. Signorelli, B. Wiesner, D. Fessas, U. Scheler, B. Voit, *J. Maly*, *Biochim. Biophys. Acta*, *Biomembranes* **2015**, 1848, 1490–1501.

[18] R. A. Rajewski, V. J. Stella, *J. Pharm. Sci*. **1996**, 85, 1142–1169.

[19] D. M. Pereira, P. Valentão, P. B. Andrade, *Mar. Drugs* **2014**, 12, 6014–6027.

[20] L. Liu, Y. Bai, N. Sun, L. Xia, T. L. Lowary, J. S. Klassen, *Chem. Eur. J*. **2012**, 18, 12059–12067.

[21] M. H. Mohamed, L. D. Wilson, J. V. Headley, K. M. Peru, *Phys. Chem. Chem. Phys*. **2011**, 13, 1112–1122.

[22] J. Xu, W. X. Zhao, Y. W. Ning, M. Bashari, F. F. Wu, H. Y. Chen, N. Yang, Z. Y. Jin, B. C. Xu, L. X. Zhang, X. M. Xu, *Carbohydr. Polym*. **2013**, 92, 1633–1640.

[23] W. C. Obiro, S. Sinha Ray, M. N. Emmambux, *Food Rev. Int*. **2012**, 28, 412–438.

[24] W. I. Weis, K. Drickamer, *Annu. Rev. Biochem* **1996**, 65, 441–473.

[25] T. L.-G. Carlson, K. Larsson, N. Dinh-Nguyen, N. Krog, *Starch* **1979**, 31, 222–224.

[26] M. Winger, M. Christen, W. F. van Gunsteren, *Int. J. Carbohydr. Chem*. **2009**, 2009, article ID 307695.

[27] O. Nimz, K. Gessler, I. Usón, G. M. Sheldrick, W. Saenger, *Carbohydr. Res*. **2004**, 339, 1427–1437.

[28] J. A. Putseys, L. Lamberts, J. A. Delcour, *J. Cereal Sci*. **2010**, 51, 238–247.

[29] L. Xia, T. L. Lowary, *Biopolymers* **2013**, 99, 697–712.

[30] M. Jackson, P. J. Brennan, *J. Biol. Chem*. **2009**, 284, 1949–1953.

[31] K. K. Yabusaki, C. E. Ballou, *Proc. Natl. Acad. Sci. U.S.A.* **1978**, 75, 691–695.

[32] J. E. Maggio, *Proc. Natl. Acad. Sci. U.S.A.* **1980**, 77, 2582–2586.

[33] M. Ilton, A. W. Jevans, E. D. McCarthy, D. Vance, H. B. White, 3rd, K. Bloch, *Proc. Natl. Acad. Sci. U.S.A.* **1971**, 68, 87–91.

[34] H. Knoche, T. W. Esders, K. Koths, K. Bloch, *J. Biol. Chem*. **1973**, 248, 2317–2322.

[35] H.-S. Cheon, Y. Wang, J. Ma, Y. Kishi, *ChemBioChem* **2007**, 8, 353–359.

[36] K. K. Yabusaki, R. E. Cohen, C. E. Ballou, *J. Biol. Chem*. **1979**, 254, 7282–7286.

[37] K. Gessler, I. Usón, T. Takaha, N. Krauss, S. M. Smith, S. Okada, G. M. Sheldrick, W. Saenger, *Proc. Natl. Acad. Sci. U.S.A.* **1999**, 96, 4246–4251.

[38] S. Zabar, U. Lesmes, I. Katz, E. Shimoni, H. Bianco-Peled, *Food Hydrocolloids* **2010**, 24, 347–357.

[39] J. Karkalas, S. Ma, W. R. Morrison, R. A. Pethrick, *Carbohydr. Res*. **1995**, 268, 233–247.

[40] G. Jovanovich, M. C. Añón, *Biopolymers* **1999**, 49, 81–89.

[41] T. A. Siswoyo, N. Morita, *Food Res. Int*. **2002**, 35, 737–744.

[42] A. Gunaratne, H. Corke, *Carbohydr. Polym*. **2007**, 68, 226–234.

[43] R. A. Pethrick, M. Song, *Carbohydr. Polym*. **2013**, 92, 1530–1538.

[44] I. A. Rose, K. R. Hanson, K. D. Wilkinson, M. J. Wimmer, *Proc. Natl. Acad. Sci. U.S.A.* **1980**, 77, 2439–2441.

[45] M. C. Godet, A. Buléon, V. Tran, P. Colonna, Carbohydr. Polym. **1993**, 21, 91–95.

[46] M. C. Godet, V. Tran, P. Colonna, A. Buleon, M. Pezolet, *Int. J. Biol. Macromol*. **1995**, 17, 405–408.

[47] F. W. Lichtenthaler, S. Immel, *Tetrahedron: Asymmetry* **1994**, 5, 2045–2060.

[48] M. Fukudome, T. Shiratani, Y. Nogami, D.-Q. Yuan, K. Fujita, *Org. Lett*. **2006**, 8, 5733–5736.

[49] S. R. Beeren, S. Meier, O. Hindsgaul, *Chem. Eur. J*. **2013**, 19, 16314–16320.

[50] L. Liu, E. N. Kitova, J. S. Klassen, *J. Am. Soc. Mass Spectrom*. **2011**, 22, 310–318.

[51] R. C. Dunbar, T. B. McMahon, *Science* **1998**, 279, 194–197.

[52] W. D. Price, P. D. Schnier, R. A. Jockusch, E. F. Strittmatter, E. R. Williams, *J. Am. Chem. Soc*. **1996**, 118, 10640–10644.

[53] L. Liu, D. Bagal, E. N. Kitova, P. D. Schnier, J. S. Klassen, *J. Am. Chem. Soc*. **2009**, 131, 15980–15981.

[54] M. H. Abraham, *J. Am. Chem. Soc*. **1982**, 104, 2085–2094.

[55] R. Fuchs, W. K. Stephenson, *Can. J. Chem*. **1985**, 63, 349–352.

[56] L. Liu, K. Michelsen, E. N. Kitova, P. D. Schnier, J. S. Klassen, *J. Am. Chem. Soc*. **2012**, 134, 3054–3060.

[57] L. Liu, K. Michelsen, E. N. Kitova, P. D. Schnier, A. Brown, J. S. Klassen, *J. Am. Chem. Soc*. **2012**, 134, 5931–5937.

[58] D. S. Tonner, D. Thölmann, T. B. McMahon, *Chem. Phys. Lett*. **1995**, 233, 324–330.

[59] P. Lebail, A. Buleon, D. Shiftan, R. H. Marchessault, *Carbohydr. Polym*. **2000**, 43, 317–326.

[60] C. E. Snape, W. R. Morrison, M. M. Maroto-Valer, J. Karkalas, R. A. Pethrick, *Carbohydr. Polym*. **1998**, 36, 225–237.

[61] T. Wyttenbach, G. von Helden, M. T. Bowers, *J. Am. Chem. Soc*. **1996**, 118, 8355–8364.

[62] C. S. Hoaglund, Y. Liu, A. D. Ellington, M. Pagel, D. E. Clemmer, *J. Am. Chem. Soc.* **1997**, 119, 9051–9052.

[63] J. V. Hamilton, J. B. Renaud, P. M. Mayer, *Rapid Comm. Mass Spectrom*. **2012**, 26, 1591–1595.

[64] D. P. Smith, T. W. Knapman, I. Campuzano, R. W. Malham, J. T. Berryman, S. E. Radforda, A. E. Ashcrofta, *Eur. J. Mass Spectrom*. **2009**, 15, 113–130.

[65] T. L. Hwang, A. J. Shaka, *J. Am. Chem. Soc*. **1992**, 114, 3157–3159.

[66] D. A. Case, T. A. Darden, T. E. Cheatham III, C. L. Simmerling, J. Wang, R. E. Duke, R. Luo, R. C. Walker, W. Zhang, K. M. Merz, B. Roberts, S. Hayik, A. Roitberg, G. Seabra, J. Swails, A. W. Götz, I. Kolossváry, K. F. Wong, F. Paesani, J. Vanicek, R. M. Wolf, J. Liu, X. Wu, S. R. Brozell, T. Steinbrecher, H. Gohlke, Q. Cai, X. Ye, J. Wang, M.-J. Hsieh, G. Cui, D. R. Roe, D. H. Mathews, M. G. Seetin, R. Salomon-Ferrer, C. Sagui, V. Babin, T. Luchko, S. Gusarov, A. Kovalenko, P. A. Kollman, University of California, San Fancisco, CA, **2012**.

[67] R. Salomon-Ferrer, D. A. Case, R. C. Walker, *WIREs Comput. Mol. Sci*. **2013**, 3, 198–210.

[68] K. N. Kirschner, A. B. Yongye, S. M. Tschampel, J. González-Outeiriño, C. R. Daniels, B. L. Foley, R. J. Woods, *J. Comput. Chem*. **2008**, 29, 622–655.

[69] J. M. Wang, R. M. Wolf, J. W. Caldwell, P. A. Kollman, D. A. Case, *J. Comput. Chem.* **2004**, 25, 1157–1174.

[70] W. L. Jorgensen, J. Chandrasekhar, J. D. Madura, R. W. Impey, M. L. Klein, *J. Chem. Phys*. **1983**, 79, 926–935.

[71] S. A. Adelman, J. D. Doll, *J. Chem. Phys*. **1976**, 64, 2375–2388.

[72] T. Darden, D. York, L. Pedersen, *J. Chem. Phys*. **1993**, 98, 10089–10092.

[73] M. Mesleh, J. Hunter, A. Shvartsburg, G. Schatz, M. Jarrold, J. *Phys. Chem*. 1996, 100, 16082–16086.

[74] A. A. Shvartsburg, M. F. Jarrold, *Chem. Phys. Lett.* **1996**, 261, 86–91.

[75] W. Humphrey, A. Dalke, K. Schulten, *Journal of Molecular Graphics* **1996**, 14, 33–38.

[76] B. T. Ruotolo, J. L. Benesch, A. M. Sandercock, S.-J. Hyung, C. V. Robinson, *Nat. Protoc*. **2008**, 3, 1139–1152.

[77] C. Uetrecht, R. J. Rose, E. van Duijn, K. Lorenzen, A. J. Heck, *Chem. Soc. Rev*. **2010**, 39, 1633–1655.

[78] J. Wildgoose, K. Giles, S. Pringle, S. Koeniger, S. Valentine, R. Bateman, D. Clemmer, in Proceedings of the 54th ASMS Conference on Mass Spectrometry and Allied Topics, American Soceity for Mass Spectrometry, Seattle, WA, **2006**, p. Abstract 064.

Table 1. Association constants (K_a) for the (MMP + FA) complexes and Arrhenius parameters (E_a, A) for the loss of neutral FA from deprotonated $(MMP + FA)^{2-}$ ions in the gas phase.[a]

FA	K_a (M^{-1})	E_a (kcal mol^{-1})	A (s^{-1})
LA	$(1.4 \pm 0.3) \times 10^4$	21.5 ± 0.5	$10^{11.7\pm0.3}$
MA	$(4.5 \pm 0.5) \times 10^4$	26.2 ± 0.8	$10^{14.2\pm0.4}$
PA	$(8.8 \pm 0.3) \times 10^{4\,b}$	27.9 ± 0.6	$10^{14.8\pm0.3}$
SA	$(1.4 \pm 0.5) \times 10^5$	29.7 ± 0.3	$10^{15.6\pm0.2}$
SA-1	$(1.1 \pm 0.4) \times 10^5$	28.6 ± 0.5	$10^{15.4\pm0.3}$
SA-2	$(1.0 \pm 0.2) \times 10^5$	28.7 ± 1.0	$10^{15.1\pm0.6}$
SA-3	$(9.0 \pm 0.6) \times 10^4$	28.5 ± 1.2	$10^{15.0\pm0.8}$
PA-D3	n. d. [c]	26.9 ± 0.3	$10^{14.2\pm0.2}$
PA-D31	n. d. [c]	25.6 ± 0.4	$10^{13.8\pm0.2}$

[a]. Reported errors are one standard deviation. [b] Value previously reported in reference [20].

[c] n.d. ≡ not determined.

Figure captions

Scheme 1. Structures of MMP, saturated FAs, oleic acid (SA-1), linoleic acid (SA-2), linolenic acid (SA-3), palmitic acid-methyl-d_3 (PA-D3), and palmitic acid-d_{31} (PA-D31).

Figure 1. ^{1}H NMR spectrum of a solution of MMP (bottom) and MMP with PA (top) in D_2O at 27 °C showing the anomeric region, ring protons, and 3-*O*-methyl groups (labeled in blue). The chemical shifts are in Tables S1 and S2.

Figure 2. Starting MMP conformation in MD simulations looking A) down the helical axis (3-*O*-methyl groups shown as spheres) and B) at the side of the helix (residues in back colored lighter). C) and D) The same views for (MMP + LA) starting conformation (LA shown as spheres; carbons in cyan).

Figure 3. Example snapshots from MD simulations of MMP, (MMP + LA), (MMP + SA). The final conformations are representative of independent simulations run for each complex in the gas phase and in aqueous solution.

Figure 4. Plots of collision cross sections (CCS, blue) and dissociation activation energies (E_a, red) measured for the gaseous $(MMP + FA)^{2-}$ ions versus the number of methylene group in FAs (LA, MA, PA and SA). Dashed lines represent linear least-squares fits for MA, PA and SA.

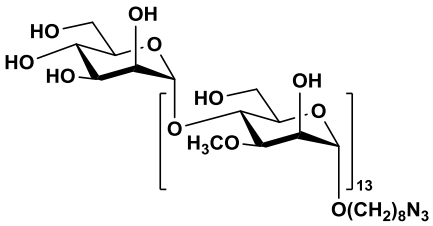

MMP

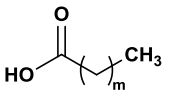

m = 10, LA
m = 12, MA
m = 14, PA
m = 16, SA

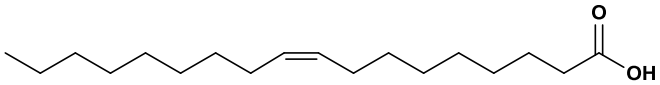

SA-1

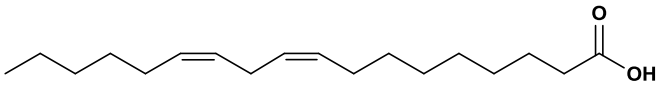

SA-2

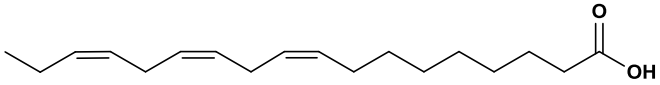

SA-3

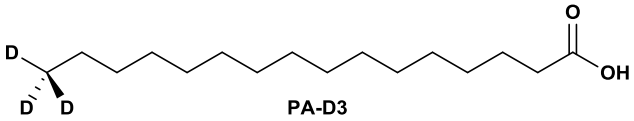

PA-D3

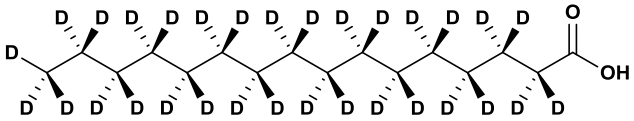

PA-D31

Scheme 1

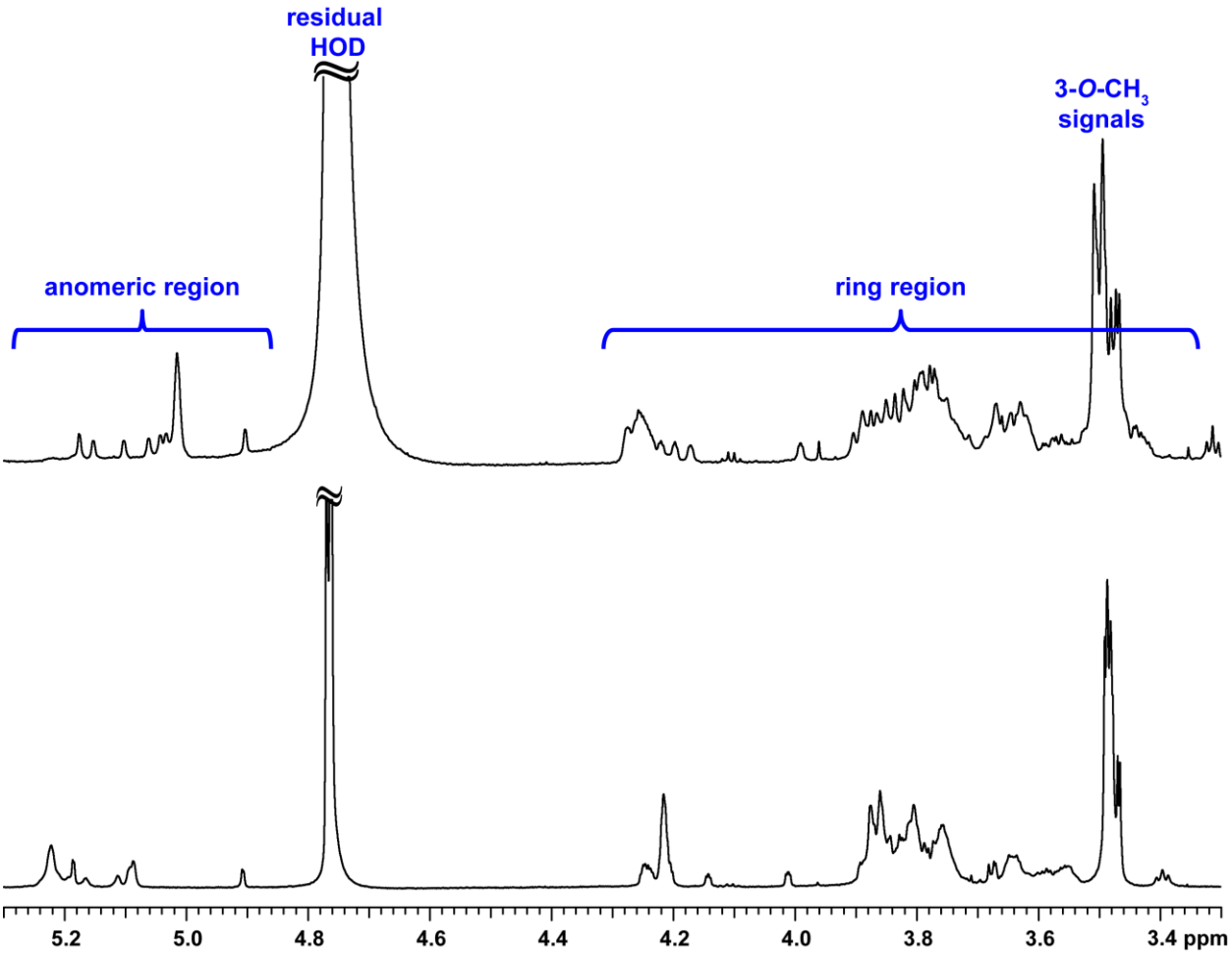
residual
HOD
3-O-CH3
signals
anomeric region
ring region
5.2
5.0
4.8
4.6
4.4
4.2
4.0
3.8
3.6
3.4 ppm

Figure 1

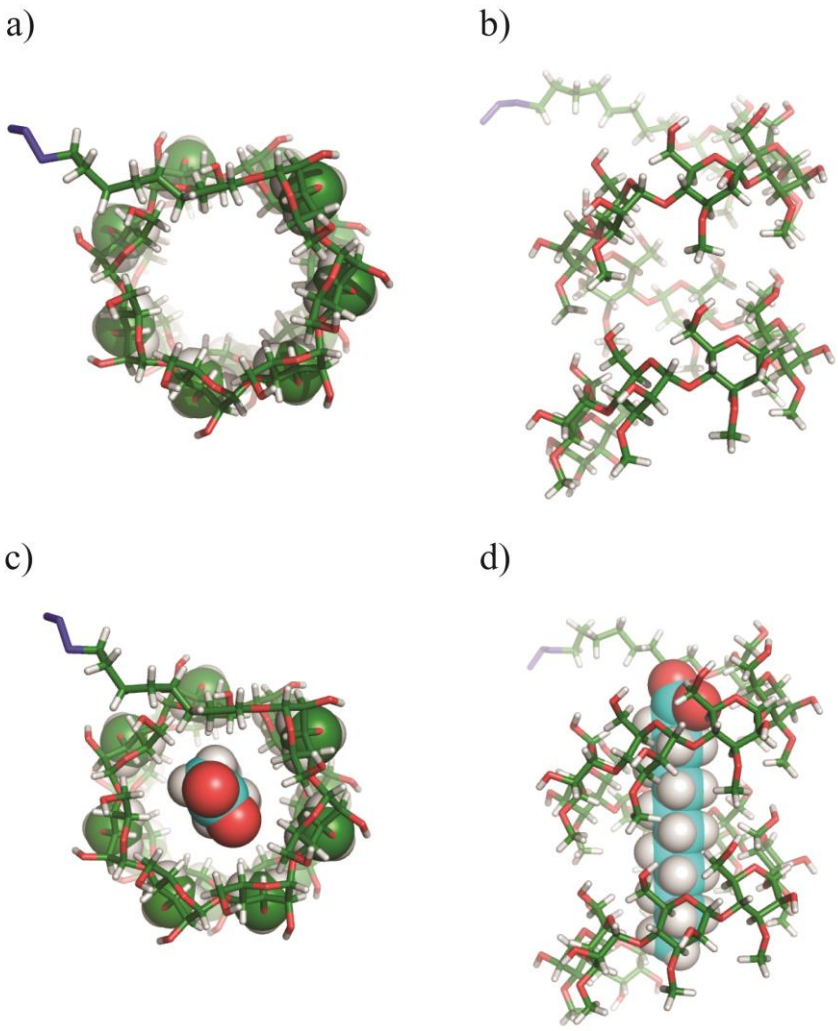

Figure 2

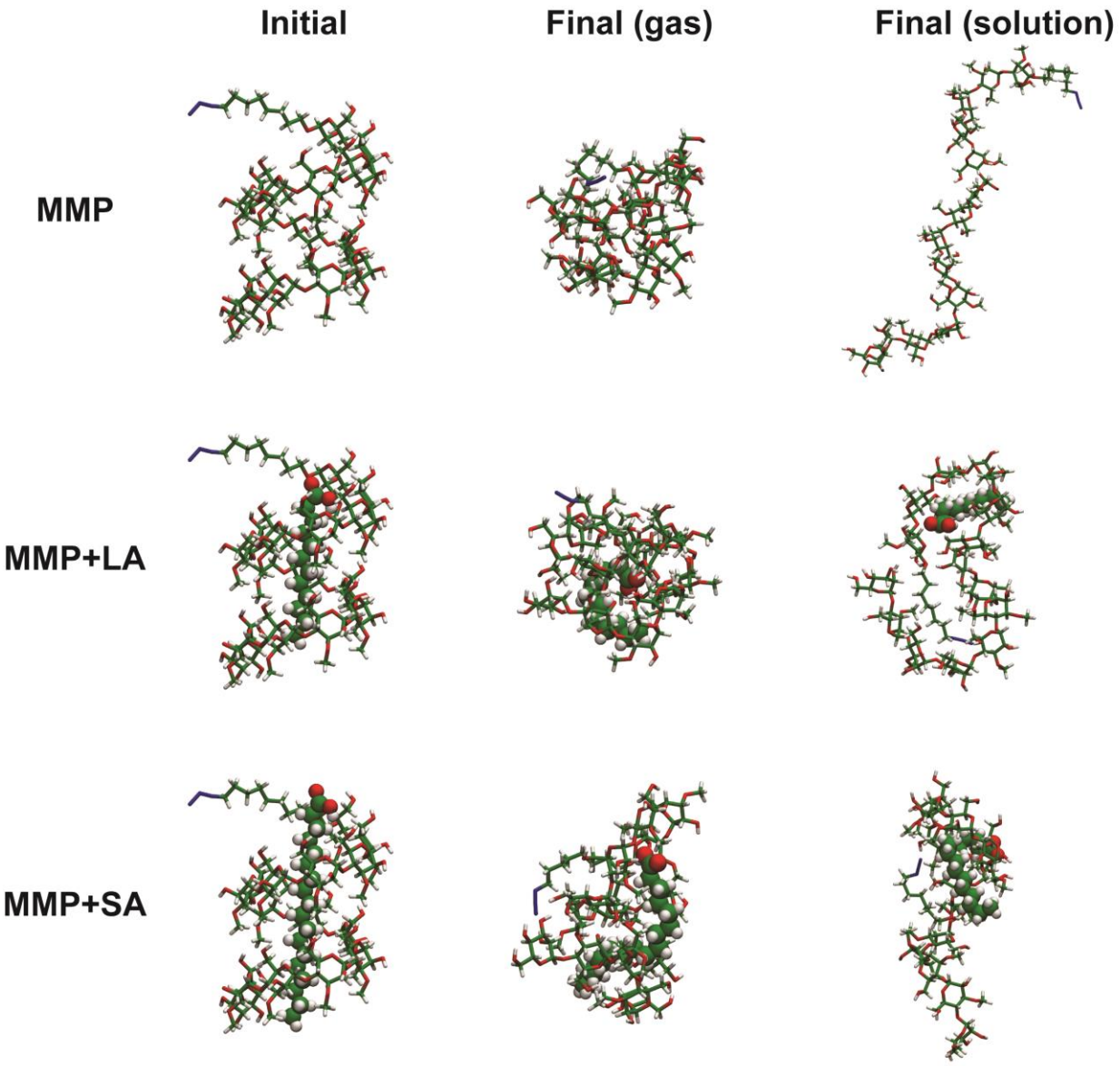

Figure 3

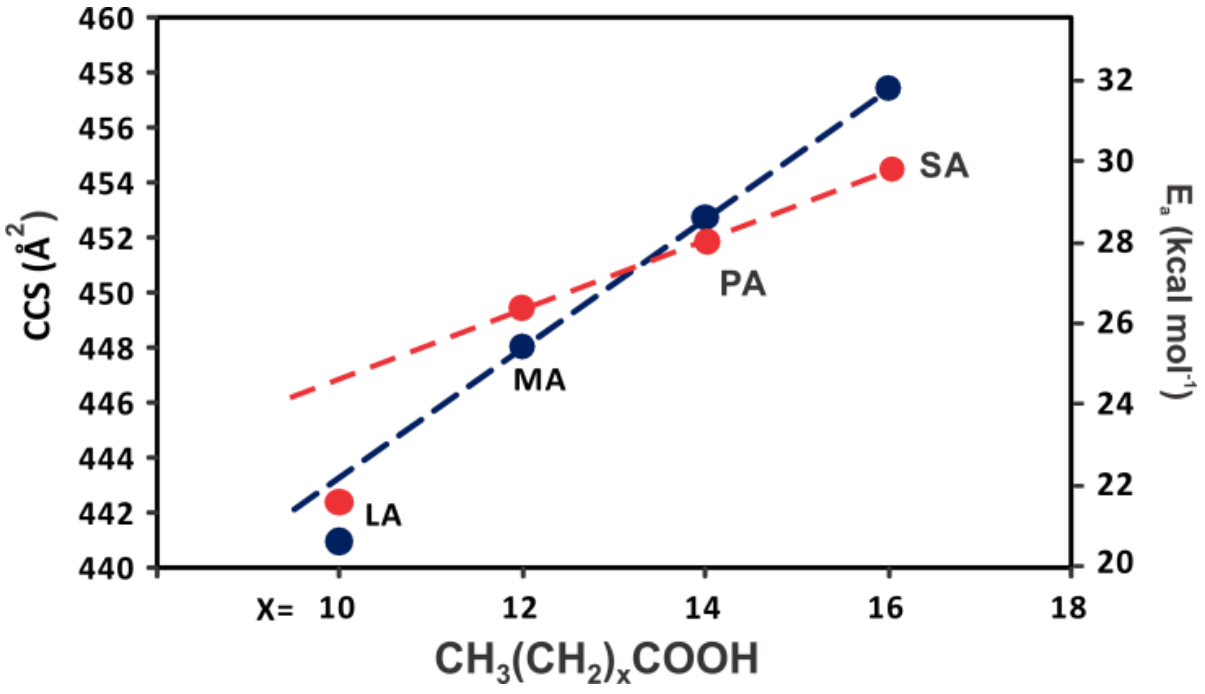
460
458
456
454
452
450
448
446
444
442
440
CCS (Å^2)
32
30
28
26
24
22
20
E_a (kcal mol^{-1})
SA
PA
MA
LA
X= 10
12
14
16
18
$CH_3(CH_2)_xCOOH$

Figure 4

Supporting Information for:

Structure and Stability of Carbohydrate–Lipid Interactions. Methylmannose Polysaccharide–Fatty Acid Complexes

Lan Liu, Iwona Siuda, Michele R. Richards, Justin Renaud, Elena N. Kitova, Paul M. Mayer, D. Peter Tieleman, Todd L. Lowary and John S. Klassen

Table of contents

Figure S1. Full ^{1}H NMR spectrum for a solution of MMP in D_2O at 27 °C. 37

Figure S2. gCOSY spectrum for a solution of MMP in D_2O at 27 °C. 38

Figure S3. gTOCSY spectrum for a solution of MMP in D_2O at 27 °C. 39

Figure S4. TROESY of MMP spectrum for a solution of MMP in D_2O at 27 °C. 40

Figure S5. Full ^{1}H NMR spectrum of a solution of MMP and PA in D_2O at 27 °C. 41

Figure S6. gCOSY spectrum of a solution of MMP and PA in D_2O at 27 °C. 42

Figure S7. gTOCSY spectrum of a solution of MMP and PA in D_2O at 27 °C. 43

Figure S8. TROESY spectrum of a solution of MMP and PA in D_2O at 27 °C. 44

Table S1. NMR chemical shifts measured for a solution of MMP in D_2O at 27 °C. 45

Table S2. NMR chemical shifts measured for a solution of MMP and PA in D_2O at 27 °C. 45

Figure S9. Plot of the natural logarithm of K_a values measured for the (MMP + FA) and (Lg + FA) complexes versus the number of methylene groups (x) in FA. 46

Table S3. Association constants (K_a) for binding of MMP and Lg to a series of FAs in aqueous ammonium acetate solutions measured using the proxy-protein ESI-MS assay.[a] 47

Figure S10. Example snapshots from MD simulations of MMP, (MMP + LA), (MMP + MA), and (MMP + PA). 48

Figure S11. Example snapshots from MD simulations of (MMP + SA), (MMP + SA-1), (MMP + SA-2), and (MMP + SA-3). 49

Figure S12. The radius of gyration (r_{gyr}) for 40 ns simulations of MMP^0 in aqueous solution.... 50

Figure S13. The radius of gyration (r_{gyr}) for 40 ns simulations of $(MMP^0 + LA)^-$ in aqueous solution..... 50

Figure S14. The radius of gyration (r_{gyr}) for 40 ns simulations of $(MMP^0 + MA)^-$ in aqueous solution..... 51

Figure S15. The radius of gyration (r_{gyr}) for 40 ns simulations of $(MMP^0 + PA)^-$ in aqueous solution..... 51

Figure S16. The radius of gyration (r_{gyr}) for 40 ns simulations of $(MMP^0 + SA)^-$ in aqueous solution..... 52

Figure S17. The radius of gyration (r_{gyr}) for 40 ns simulations of $(MMP^0 + SA\text{-}1)^-$ in aqueous solution..... 52

Figure S18. The radius of gyration (r_{gyr}) for 40 ns simulations of $(MMP^0 + SA\text{-}2)^-$ in aqueous solution..... 53

Figure S19. The radius of gyration (r_{gyr}) for 40 ns simulations of $(MMP^0 + SA\text{-}3)^-$ in aqueous solution..... 53

Figure S20. ESI mass spectra acquired for aqueous solutions of MMP and a series of FAs 54

Figure S21. Illustrative BIRD mass spectra measured for $(MMP + FA)^{2-}$ complexes. 55

Figure S22. Plots of the natural logarithm of the normalized abundance (Ab/Ab_o) of $(Lg + FA)^{7-}$ ions versus reaction time..... 56

Figure S23. Arrhenius plots for the loss of neutral FA from the gaseous deprotonated $(MMP + FA)^{2-}$ ions. 57

Figure S24. Plots of the natural logarithm of the normalized abundance (Ab/Ab_o) of $(MMP + PA)^{7-}$ ion versus reaction time. 58

Figure S25. ESI mass spectra acquired for aqueous solutions of (a) MMP and PA, and (b) D-MMP and PA. Illustrative BIRD mass spectra measured for (c) $(MMP + PA)^{2-}$ and (d) $(D\text{-}MMP + PA)^{2-}$..... 59

Figure S26. Plots of the normalized abundance (Ab/Ab_o) of $(MMP + PA)^{2-}$ and $(D\text{-}MMP + PA)^{2-}$ versus reaction time 60

Table S4. Collision cross section (CCS) calibration..... 61

Figure S27. (a) Plot of ln(CCS′) versus ln(tD′) for the calibrants: InsA, dT10DNA, and PS. (b) Calibration curve, based on the calibrants : InsA, dT10DNA, and PS, displayed as a linear plot of literature CCS values and final corrected drift times (tD″). 63

Table S5. Measured drift times (t_D), corrected drift times (t_D' and t_D") and collision cross sections (CCS) for deprotonated FA^-, MMP^{2-} and $(MMP + FA)^{2-}$ ions. 64

Figure S28. CCS for MMP^{2-} calculated over the 100 ns MD simulations. 65

Figure S29. CCS for $(MMP^{2-} + LA)^{2-}$ calculated over the 100 ns MD simulations. 65

Figure S30. CCS for $(MMP^{2-} + MA)^{2-}$ calculated over the 100 ns MD simulations. 66

Figure S31. CCS for $(MMP^{2-} + PA)^{2-}$ calculated over the 100 ns MD simulations. 66

Figure S32. CCS for $(MMP^{2-} + SA)^{2-}$ calculated over the 100 ns MD simulations. 67

Figure S33. CCS for $(MMP^{2-} + SA\text{-}1)^{2-}$ calculated over the 100 ns MD simulations. 67

Figure S34. CCS for $(MMP^{2-}+SA\text{-}2)^{2-}$ calculated over the 100 ns MD simulations. 68

Figure S35. CCS for $(MMP^{2-} + SA\text{-}3)^{2-}$ calculated over the 100 ns MD simulations.. 68

References: 69

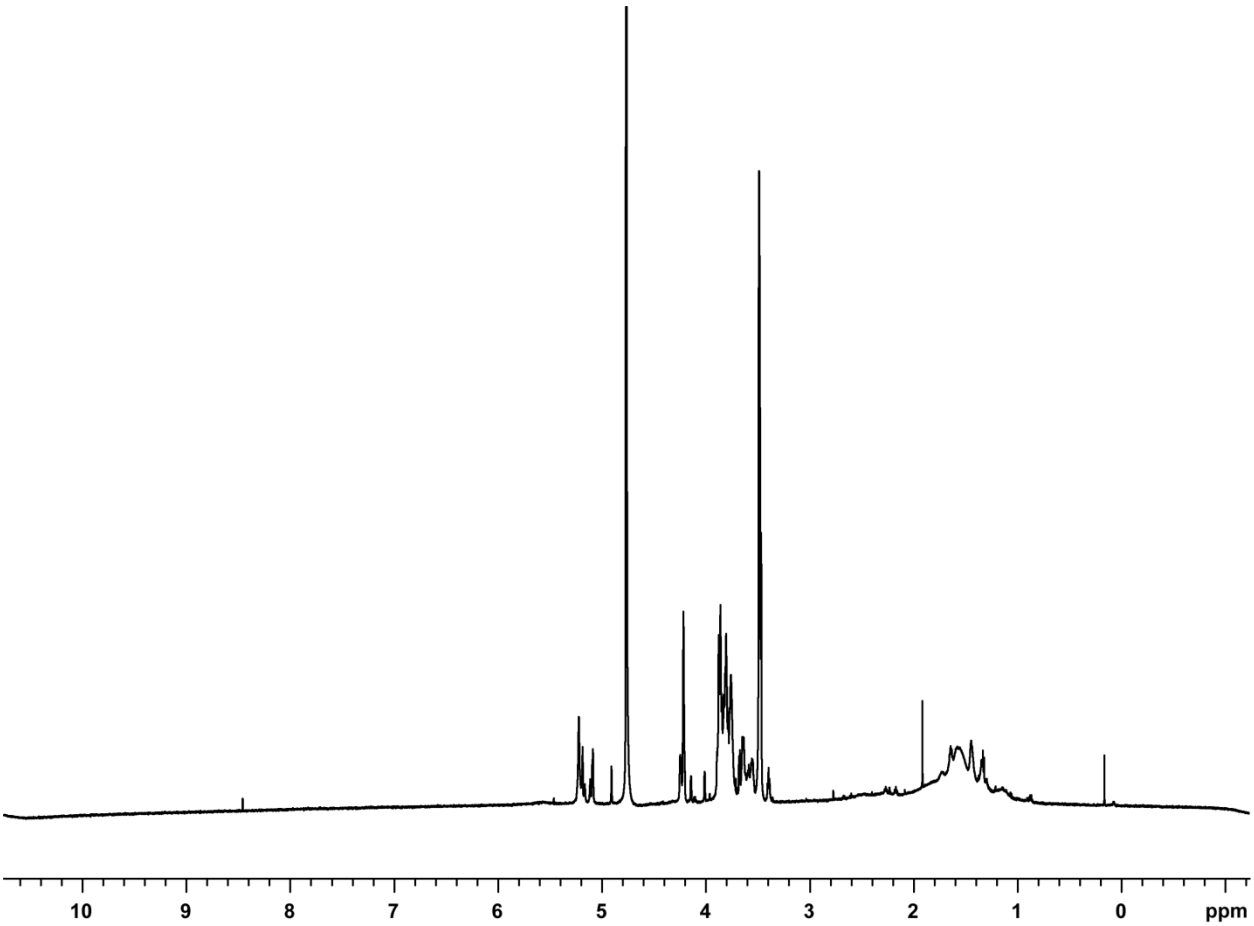

Figure S1. Full ^{1}H NMR spectrum for a solution of MMP in D_2O at 27 °C.

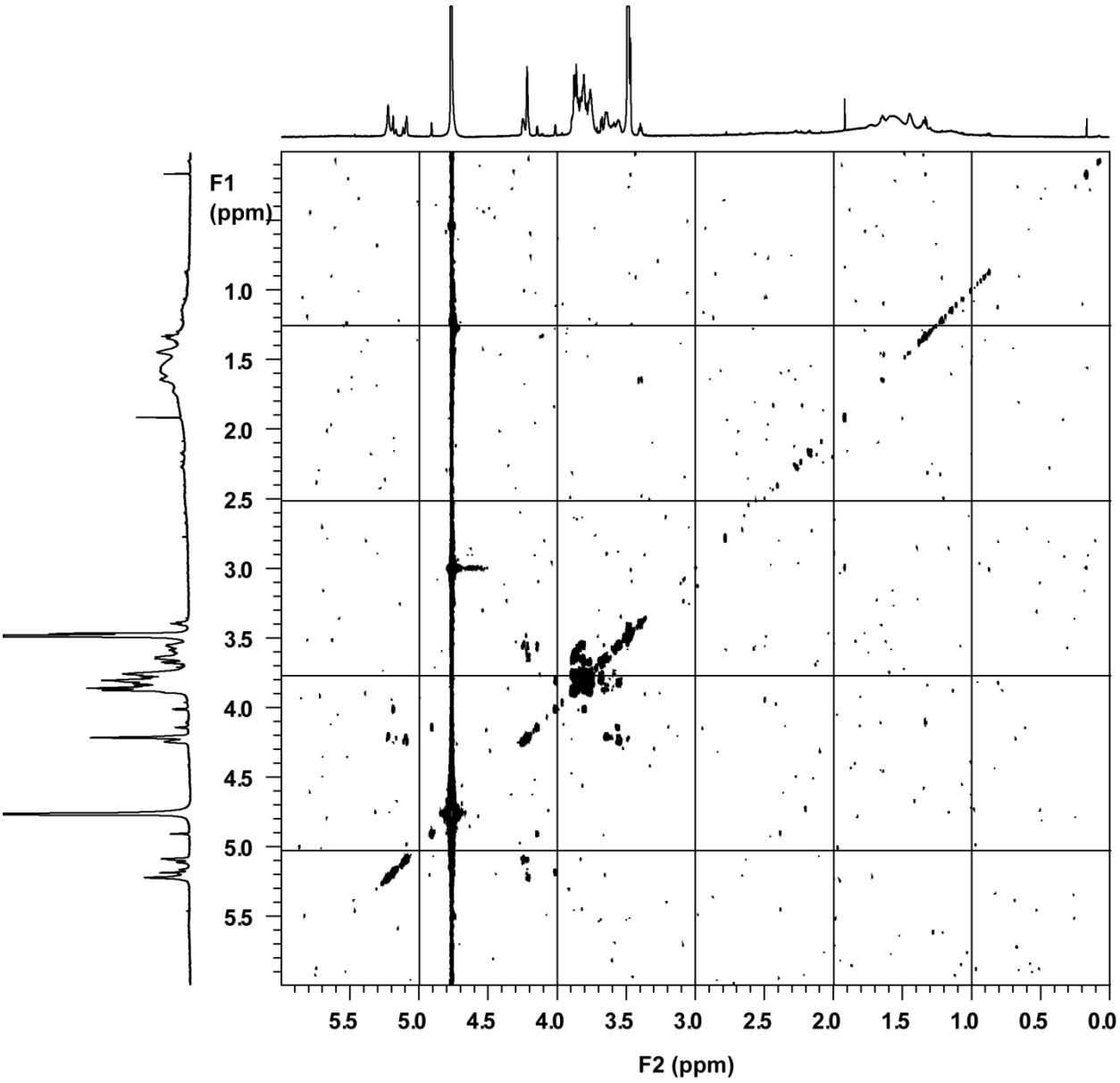

Figure S2. gCOSY spectrum for a solution of MMP in D_2O at 27 °C.

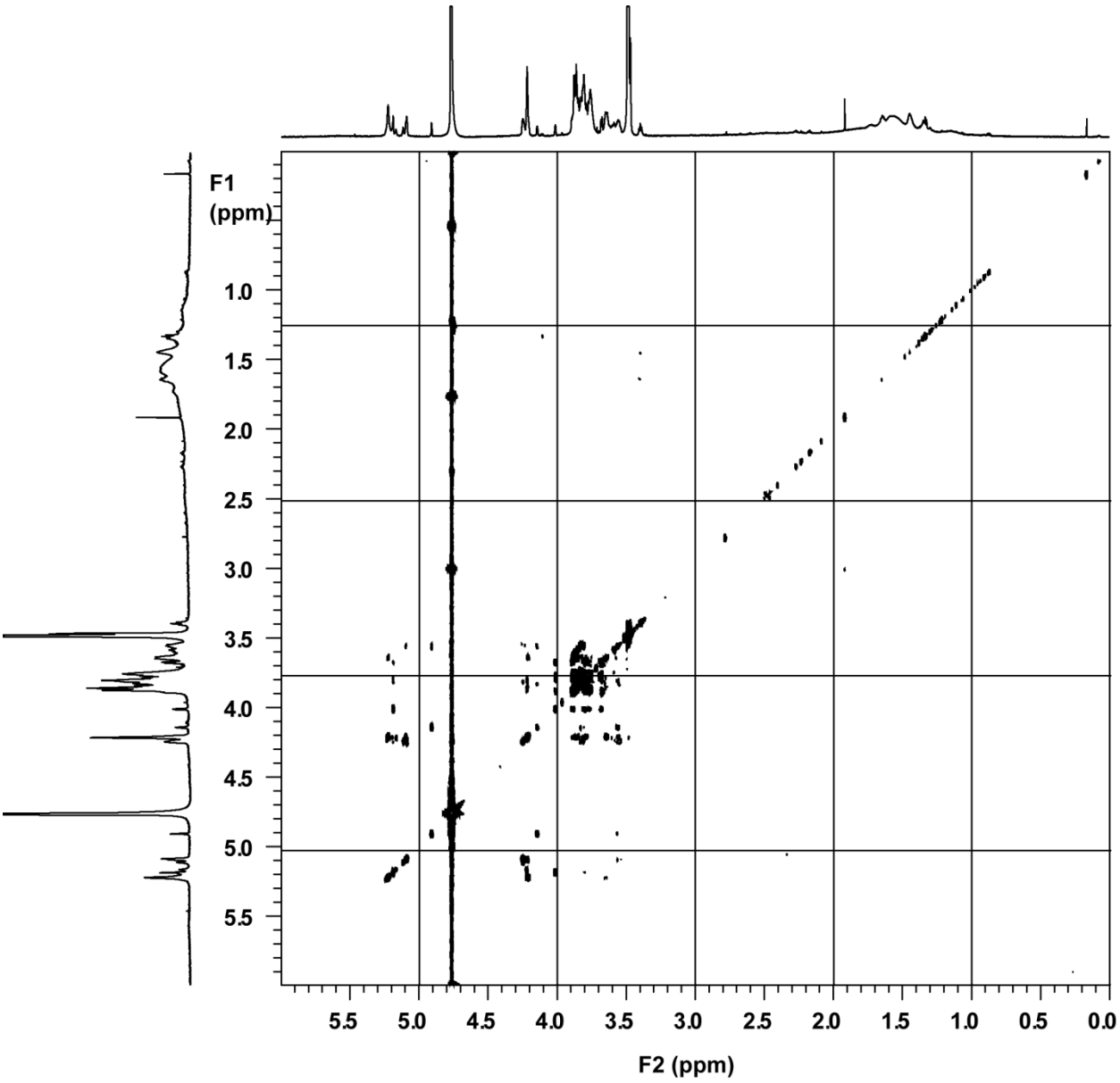

Figure S3. gTOCSY spectrum for a solution of MMP in D_2O at 27 °C.

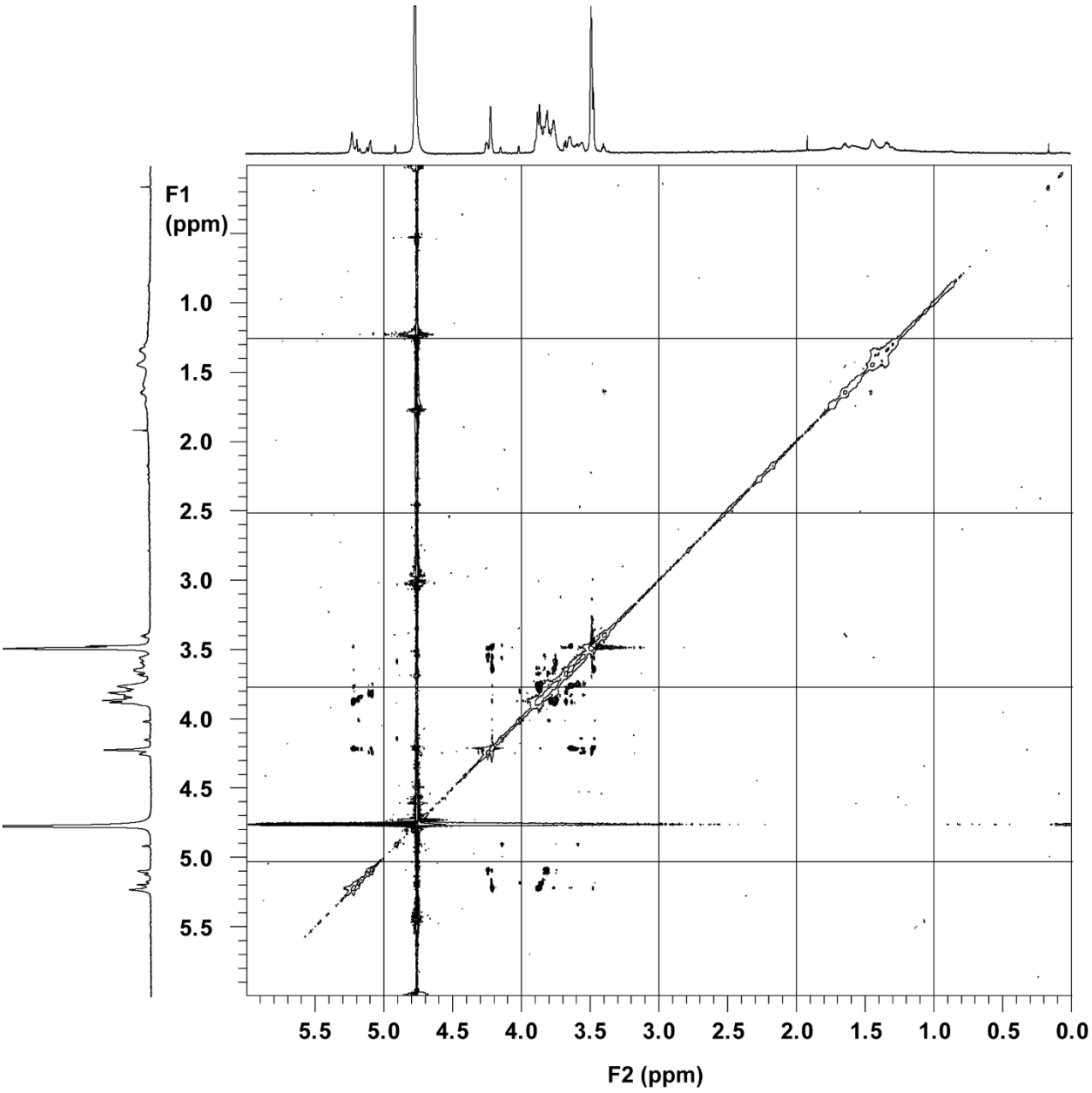

Figure S4. TROESY of MMP spectrum for a solution of MMP in D_2O at 27 °C.

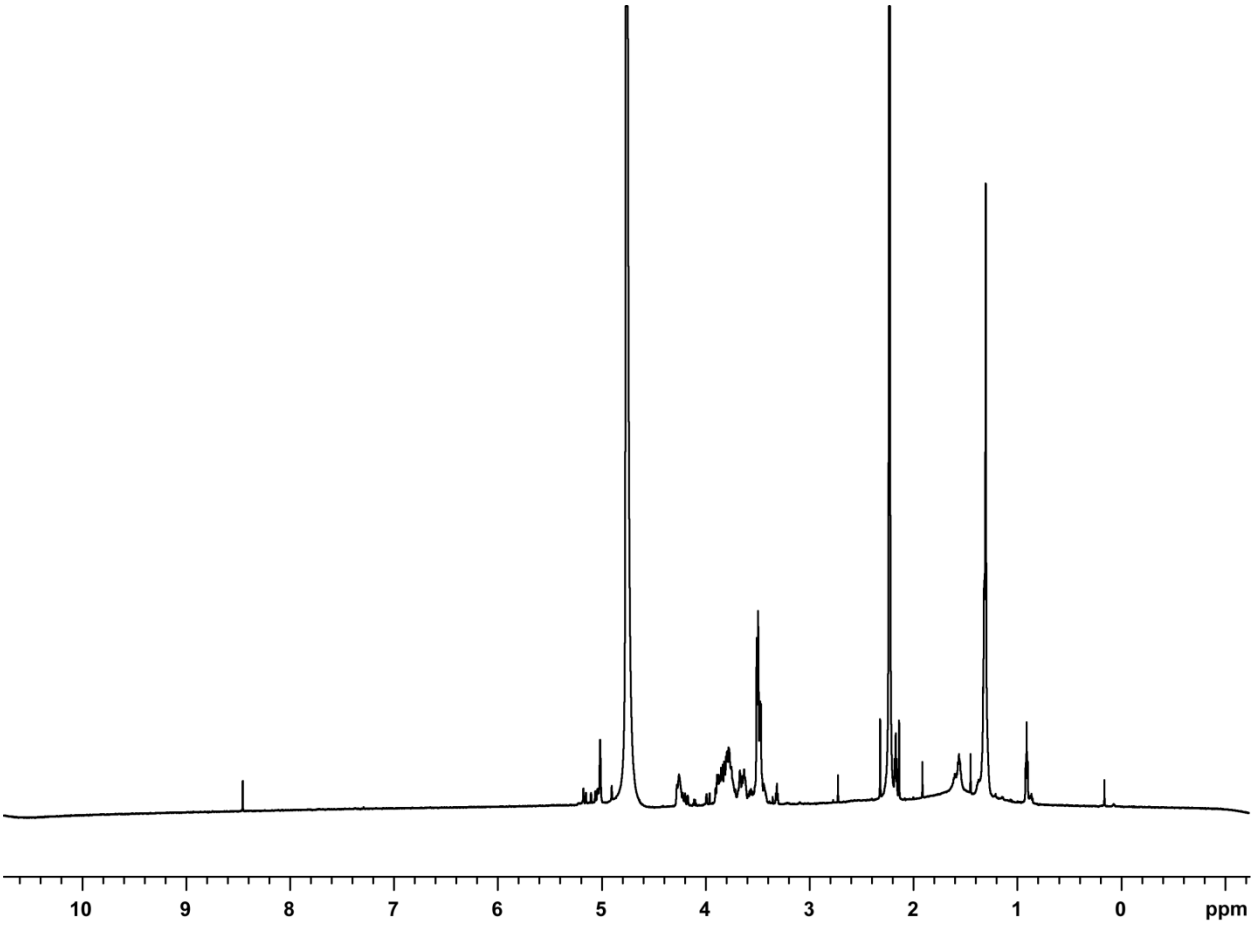

Figure S5. Full ^{1}H NMR spectrum of a solution of MMP and PA in D_2O at 27 °C.

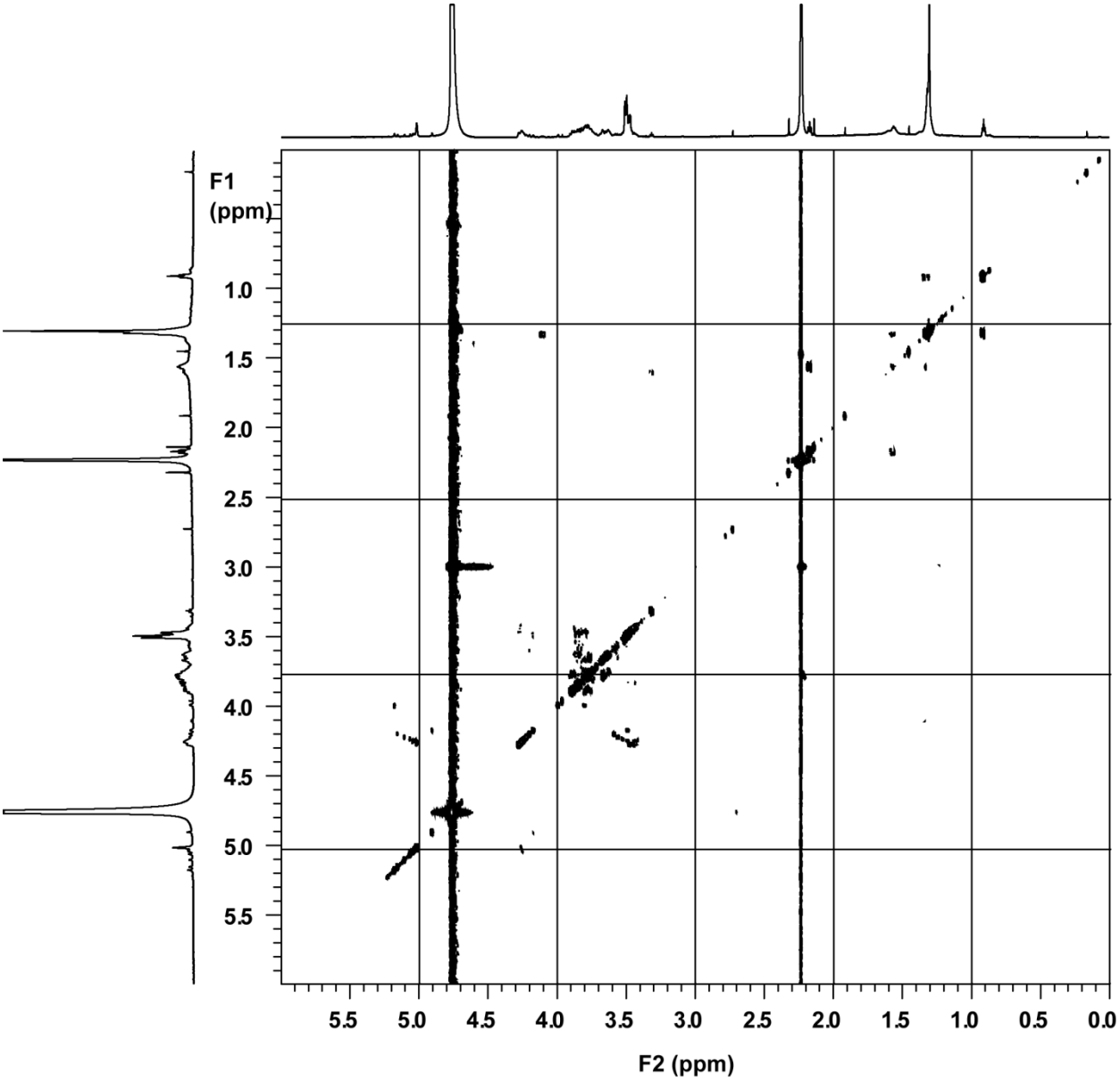

Figure S6. gCOSY spectrum of a solution of MMP and PA in D_2O at 27 °C.

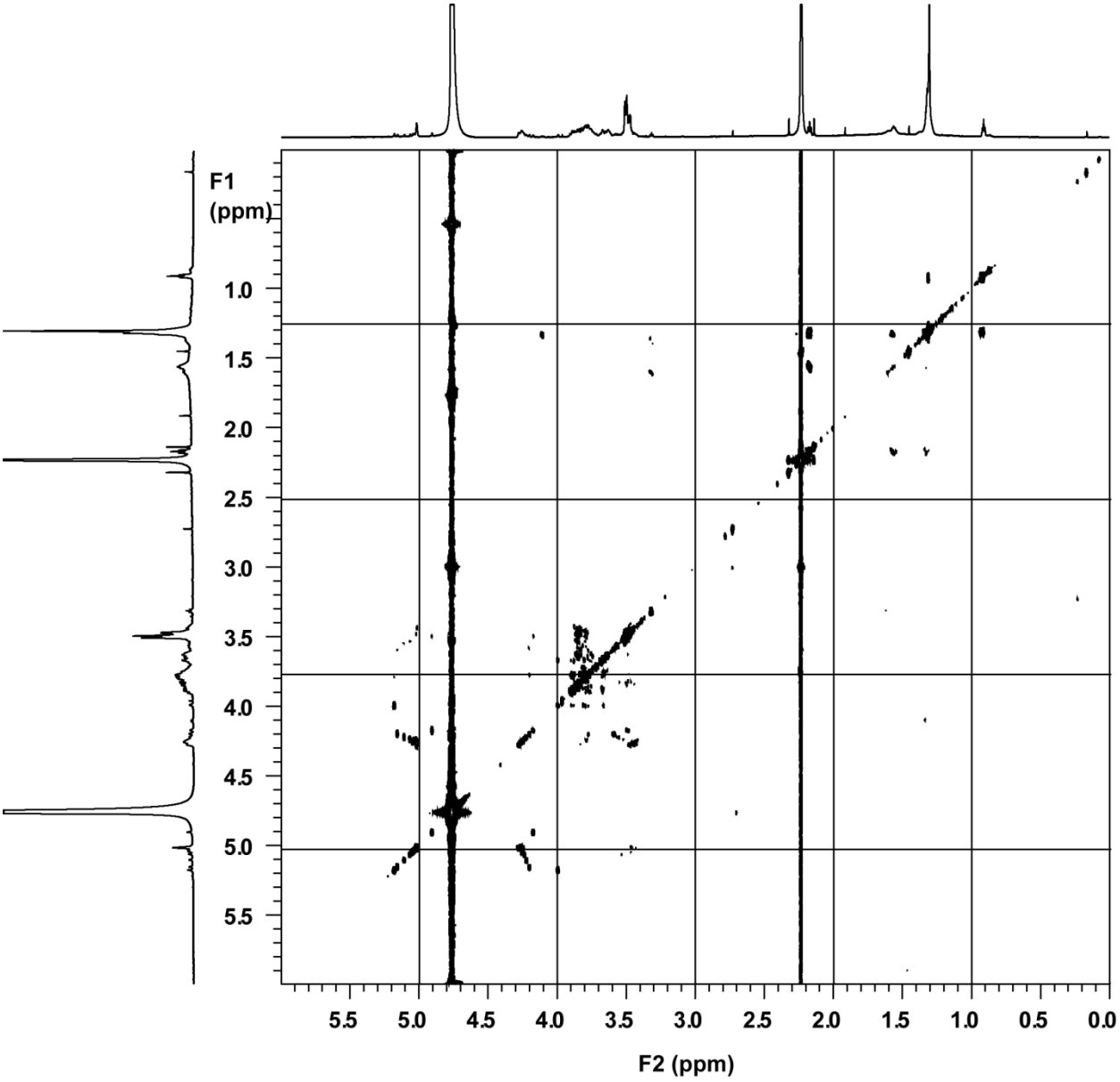

Figure S7. gTOCSY spectrum of a solution of MMP and PA in D_2O at 27 °C.

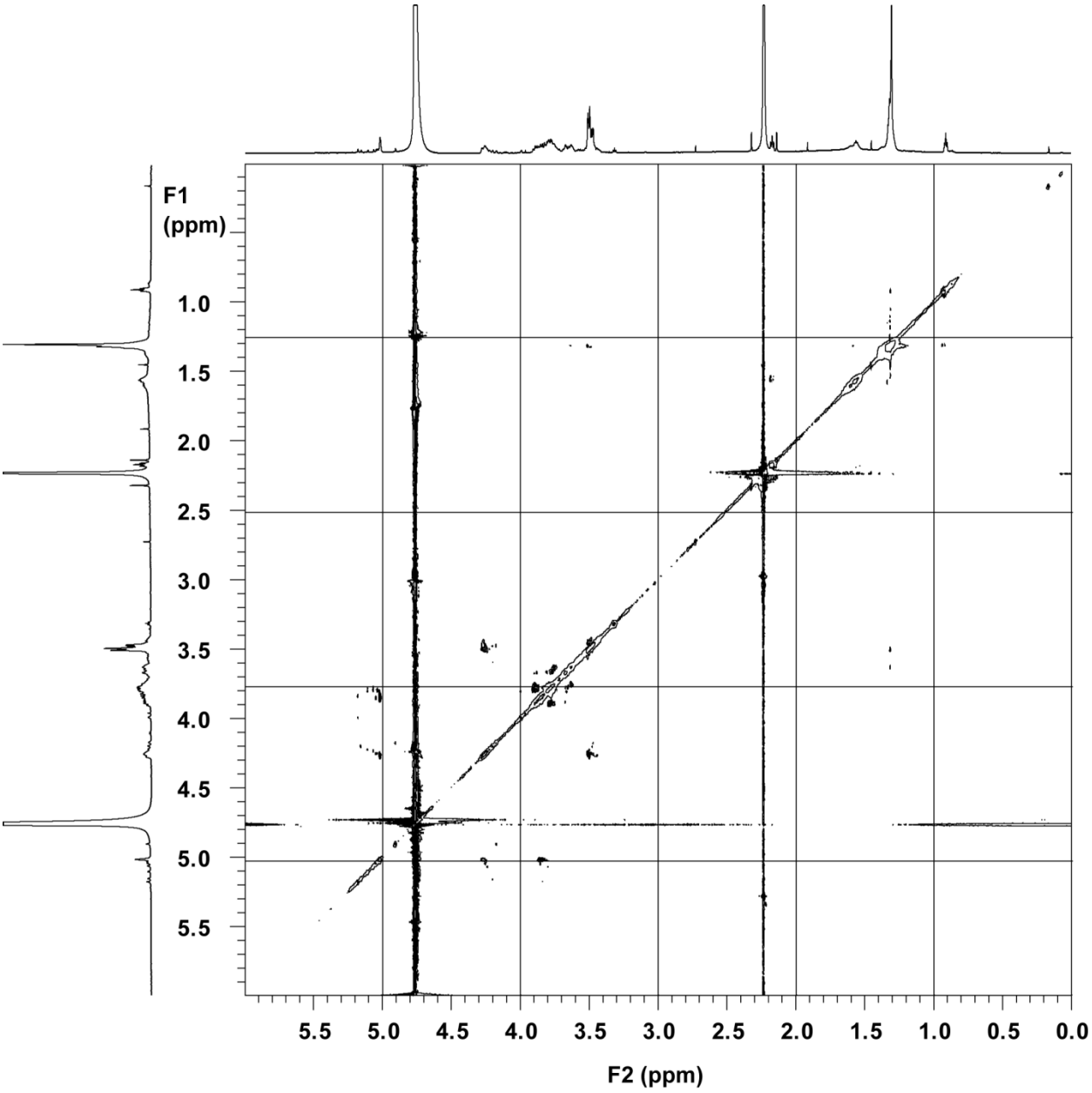

Figure S8. TROESY spectrum of a solution of MMP and PA in D_2O at 27 °C.

Table S1. NMR chemical shifts measured for a solution of MMP in D_2O at 27 °C.

H1 (ppm)	H2 (ppm) from COSY	H3 (ppm) from TOSCY	Correlated to H4 (ppm) from TROESY	
5.22	4.22	3.66	3.88	
5.19	4.02	3.82	3.87	Non-reducing end
5.16	4.23	N.D.*	3.85	
5.11	4.25	N.D.*	3.82 (weak)	
5.09(3)	4.23	3.57	3.82	
5.08(7)	4.26	N.D.*	3.82	
4.91	4.15	3.57	N.D.*	Reducing end

*N.D. = Not determined

Table S2. NMR chemical shifts measured for a solution of MMP and PA in D_2O at 27 °C.

H1 (ppm)	H2 (ppm) from COSY	H3 (ppm) from TOSCY	Correlated to H4 (ppm) from TROESY	
5.18	4.01	3.80	3.84	Non-reducing end
5.16	4.20	3.60	3.83	
5.11	4.23	3.56	3.80	
5.06	4.24	3.54	3.80	
5.05	4.25	3.49	3.86	
5.03	4.26	N.D.*	3.81	
5.02	4.27	3.50, 3.44	3.85	
4.90	3.18	3.51	N.D.*	Reducing end

*N.D. = Not determined

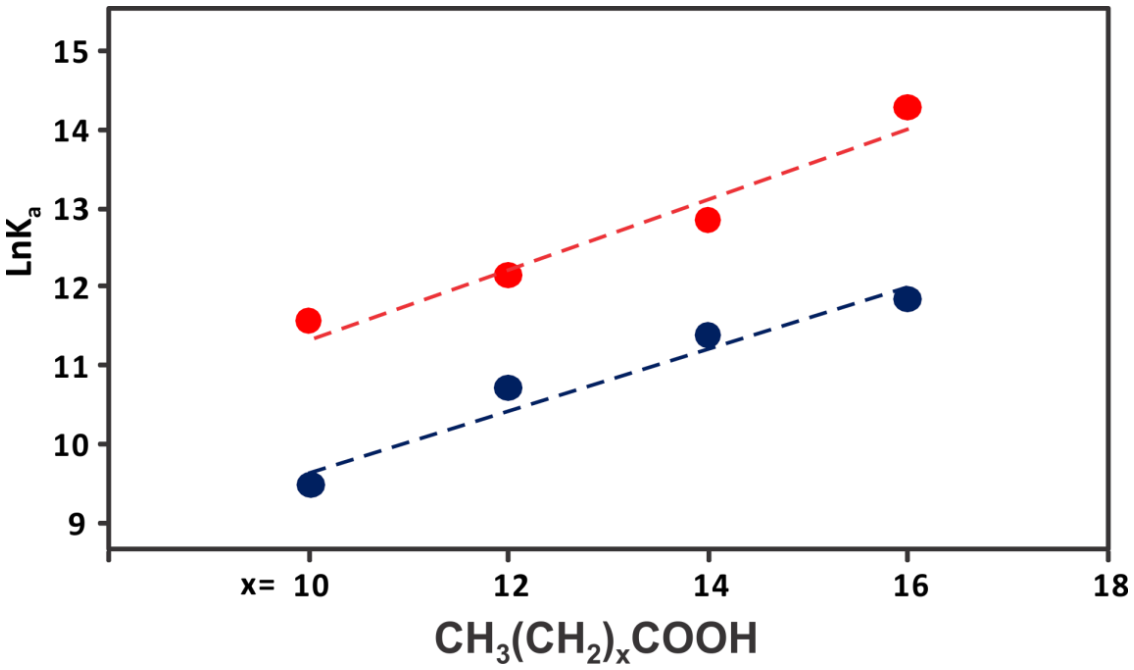

Figure S9. Plot of the natural logarithm of K_a values measured for the (MMP + FA) (●) and (Lg + FA) (●) complexes versus the number of methylene groups (x) in FA. The dashed line corresponds to linear least squares fit of the data points.

Table S3. Association constants (K_a) for binding of MMP and Lg to a series of FAs in aqueous ammonium acetate solutions (pH 8.5, 25 °C) measured using the proxy-protein ESI-MS assay.[a]

	K_a (M^{-1})	
FA	**MMP**	**Lg**
LA	$(1.4 \pm 0.3) \times 10^4$	$(1.1 \pm 0.2) \times 10^5$ [b]
MA	$(4.5 \pm 0.5) \times 10^4$	$(1.9 \pm 0.1) \times 10^5$ [b]
PA	$(8.8 \pm 0.3) \times 10^4$ [d]	$(3.8 \pm 0.1) \times 10^5$ [b]
SA	$(1.4 \pm 0.5) \times 10^5$	$(1.6 \pm 0.1) \times 10^6$ [b]
SA-1	$(1.1 \pm 0.4) \times 10^5$	$(1.9 \pm 0.2) \times 10^6$ [c]
SA-2	$(1.0 \pm 0.2) \times 10^5$	$(2.1 \pm 0.2) \times 10^6$ [c]
SA-3	$(9.0 \pm 0.6) \times 10^4$	$(2.4 \pm 0.4) \times 10^6$ [c]

a. The reported errors are one standard deviation. b. Values are taken from Liu, et al. (2011).[1] c. Values are taken from reference Liu, et al (2012a).[2] d. Values are taken from reference Liu, et al (2012b).[3]

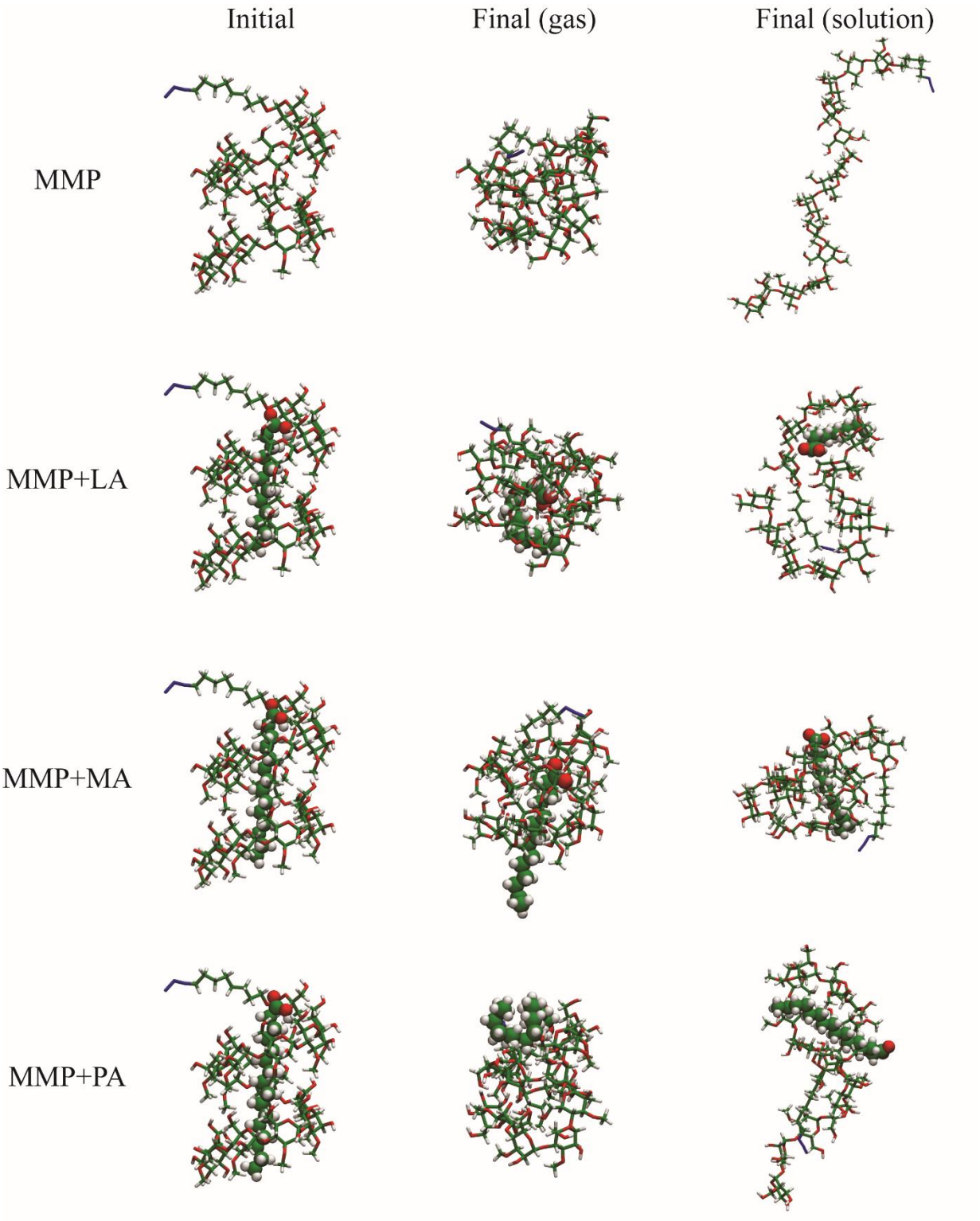

Figure S10. Example snapshots from MD simulations of MMP, (MMP + LA), (MMP + MA), and (MMP + PA). The final conformations are representative of each of the three independent simulations run for each complex in the gas phase and in aqueous solution.

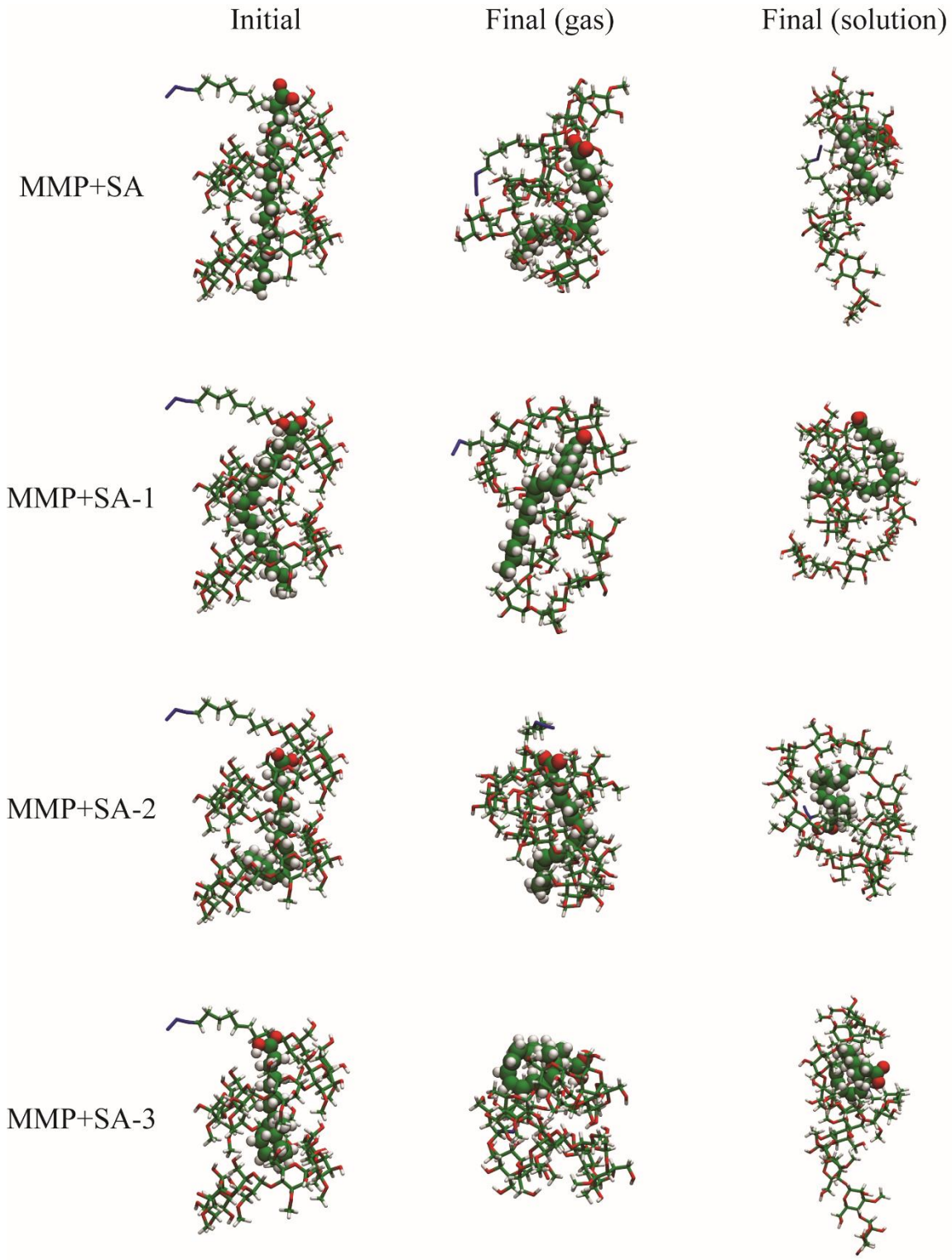

Figure S11. Example snapshots from MD simulations of (MMP + SA), (MMP + SA-1), (MMP + SA-2), and (MMP + SA-3). The final conformations are representative of each of the three independent simulations run for each complex in the gas phase and in aqueous solution.

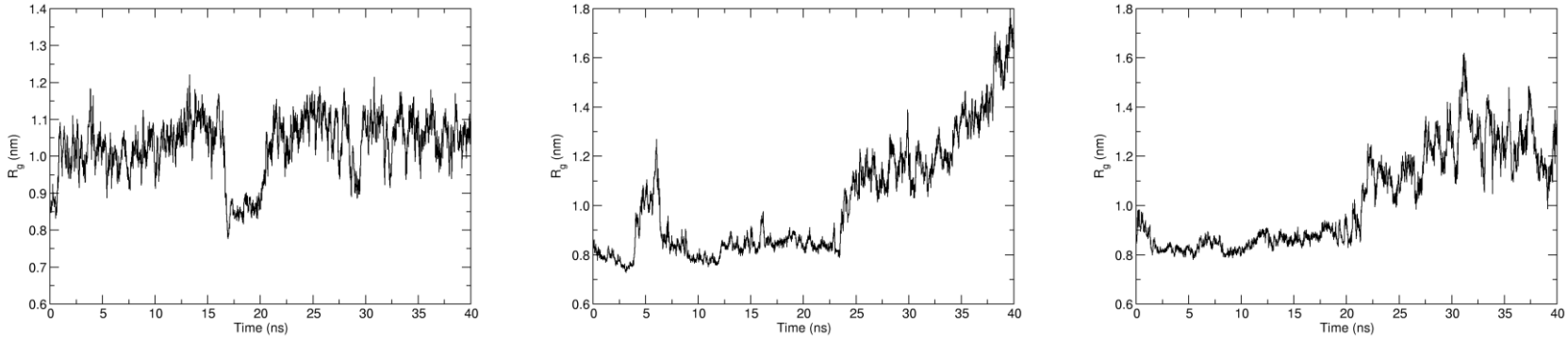

Figure S12. The radius of gyration (r_{gyr}) for 40 ns simulations of MMP^0 in aqueous solution.

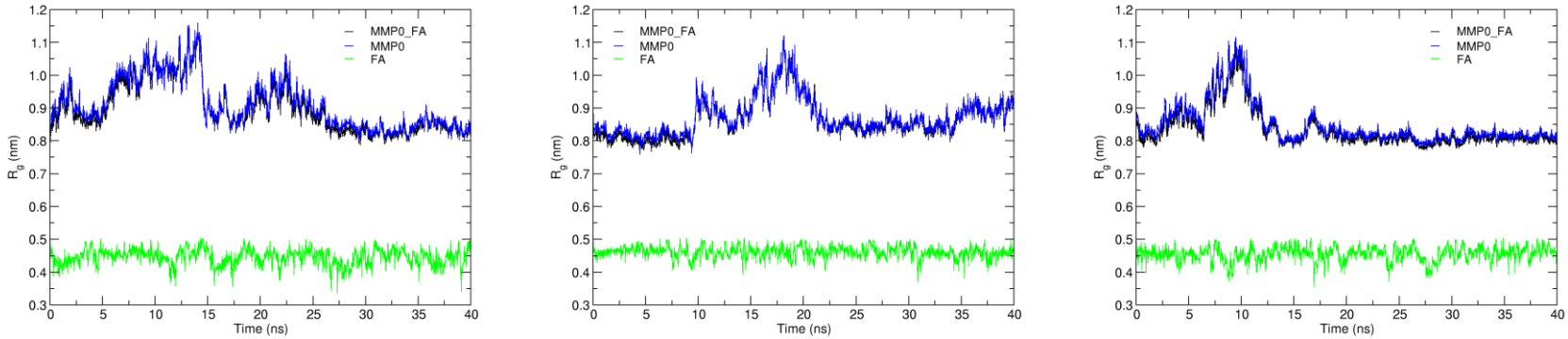

Figure S13. The radius of gyration (r_{gyr}) for 40 ns simulations of $(MMP^0 + LA)^-$ in aqueous solution. The r_{gyr} for MMP is shown in blue, for the FA chain in green, and for the (MMP + FA) complex in black.

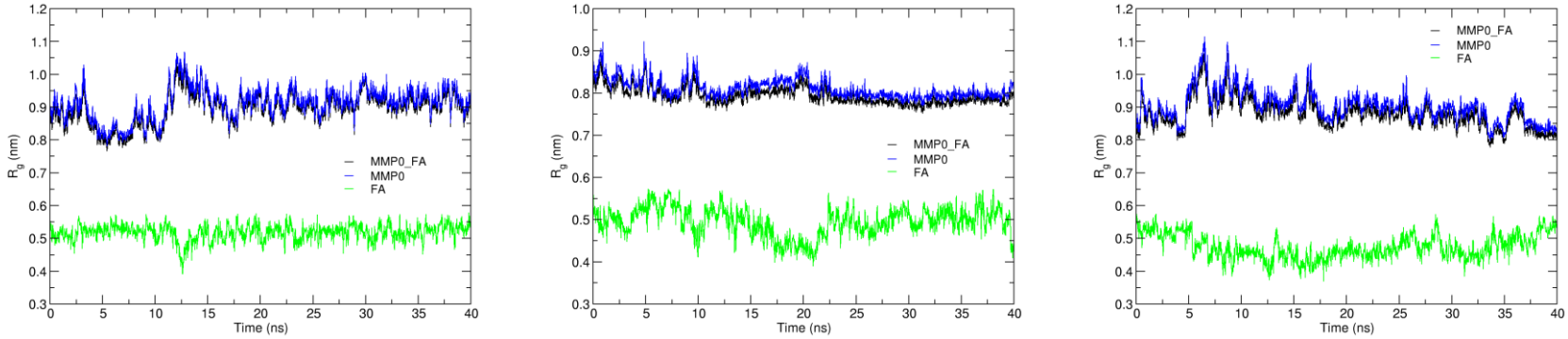

Figure S14. The radius of gyration (r_{gyr}) for 40 ns simulations of $(MMP^0 + MA)^-$ in aqueous solution. The r_{gyr} for MMP is shown in blue, for the FA chain in green, and for the (MMP + FA) complex in black.

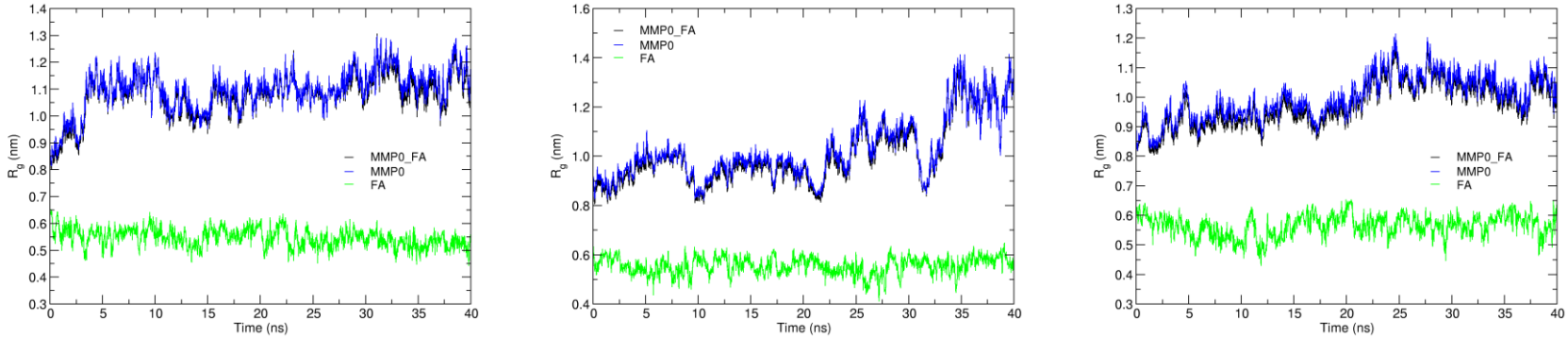

Figure S15. The radius of gyration (r_{gyr}) for 40 ns simulations of $(MMP^0 + PA)^-$ in aqueous solution. The r_{gyr} for MMP is shown in blue, for the FA chain in green, and for the (MMP + FA) complex in black.

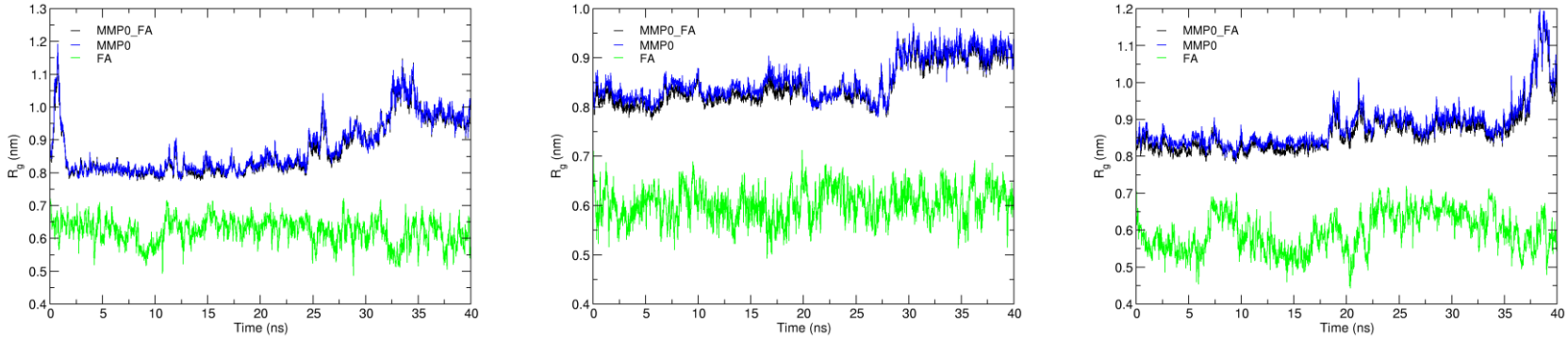

Figure S16. The radius of gyration (r_{gyr}) for 40 ns simulations of $(MMP^0 + SA)^-$ in aqueous solution. The r_{gyr} for MMP is shown in blue, for the FA chain in green, and for the (MMP + FA) complex in black.

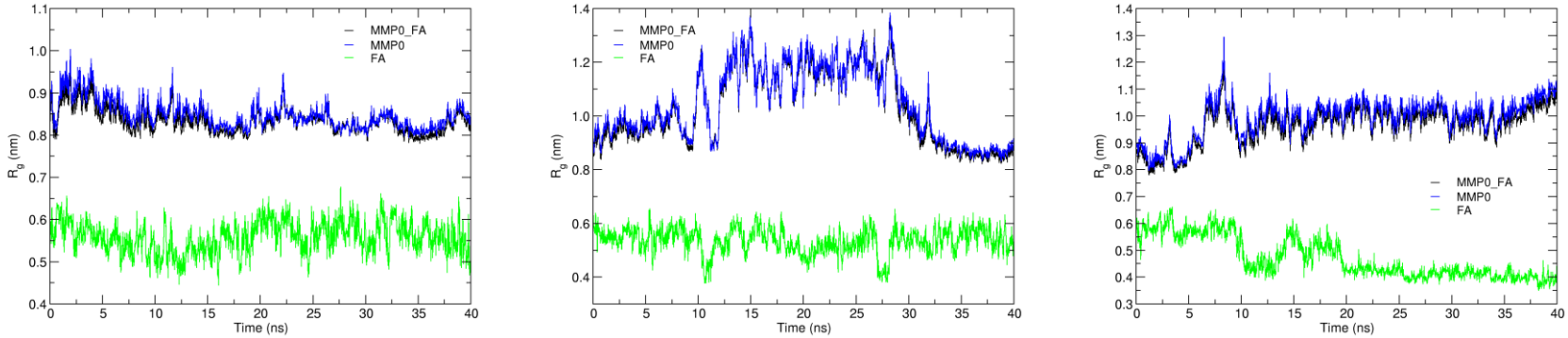

Figure S17. The radius of gyration (r_{gyr}) for 40 ns simulations of $(MMP^0 + SA\text{-}1)^-$ in aqueous solution. The r_{gyr} for MMP is shown in blue, for the FA chain in green, and for the (MMP + FA) complex in black.

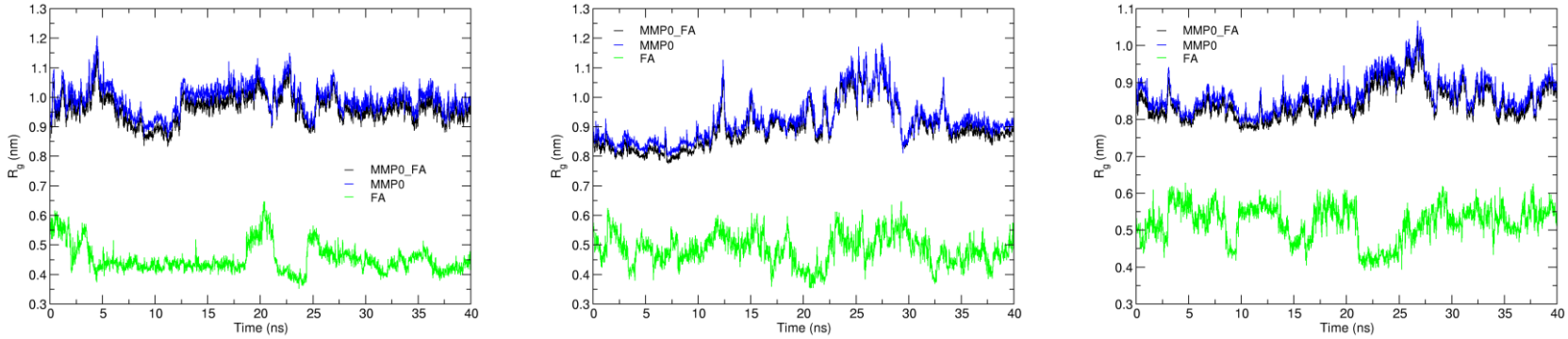

Figure S18. The radius of gyration (r_{gyr}) for 40 ns simulations of $(MMP^0 + SA\text{-}2)^-$ in aqueous solution. The r_{gyr} for MMP is shown in blue, for the FA chain in green, and for the (MMP + FA) complex in black.

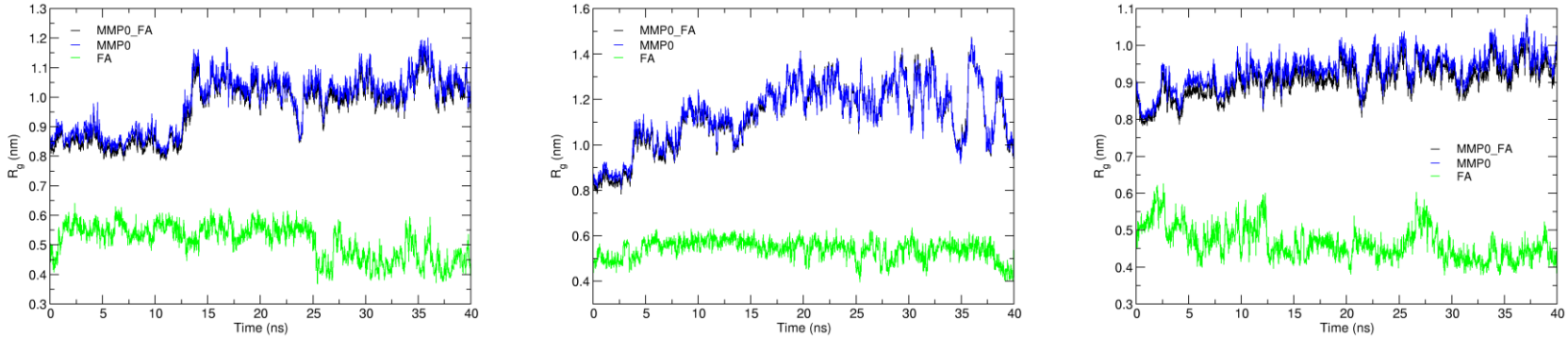

Figure S19. The radius of gyration (r_{gyr}) for 40 ns simulations of $(MMP^0 + SA\text{-}3)^-$ in aqueous solution. The r_{gyr} for MMP is shown in blue, for the FA chain in green, and for the (MMP + FA) complex in black.

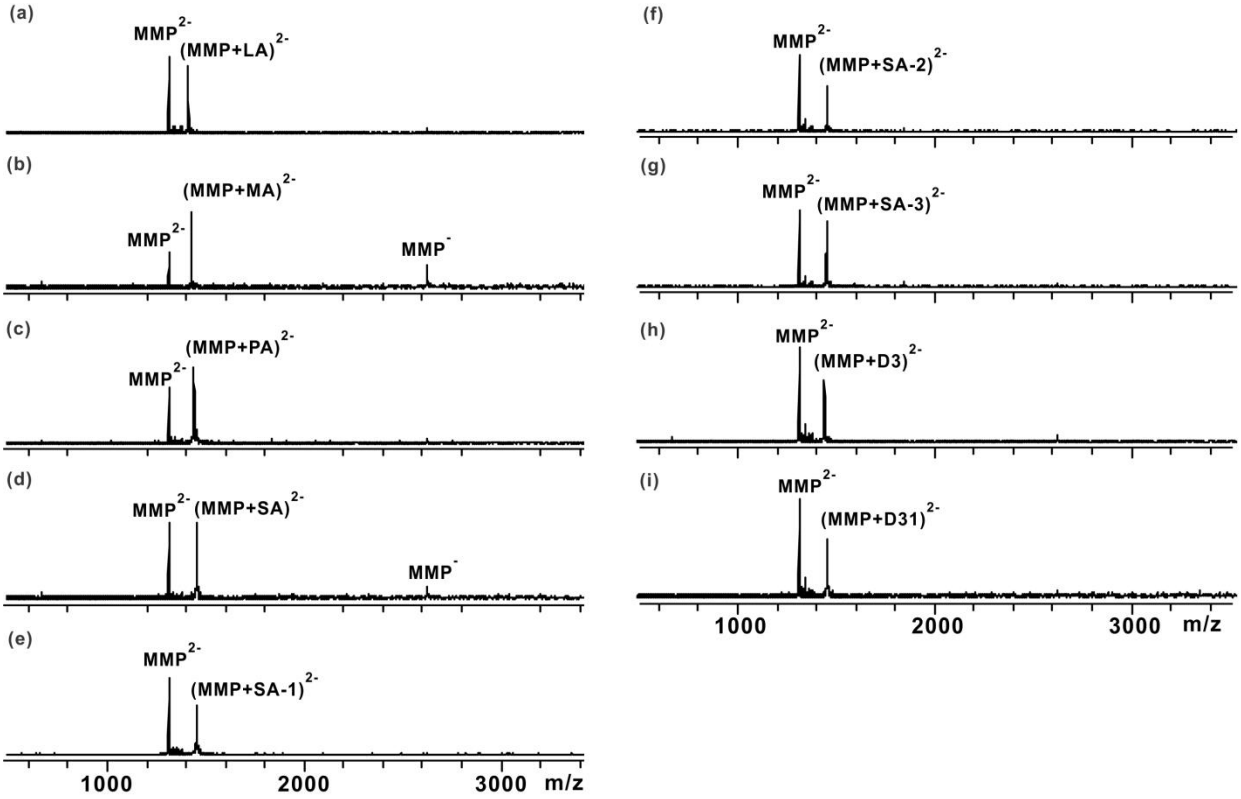

Figure S20. ESI mass spectra acquired for aqueous solutions (pH 8.5, 25 °C) of MMP (45 μM) and (a) LA (80 μM), (b) MA (50 μM, (c) PA (45 μM), (d) SA (45 μM), (e) SA-1 (50 μM), (f) SA-2 (50 μM, (g) SA-3 (40 μM), (h) PA-D3 (40 μM), and (i) PA-D31 (50 μM). Each solution contained 10 mM ammonium acetate and 10 mM imidazole.

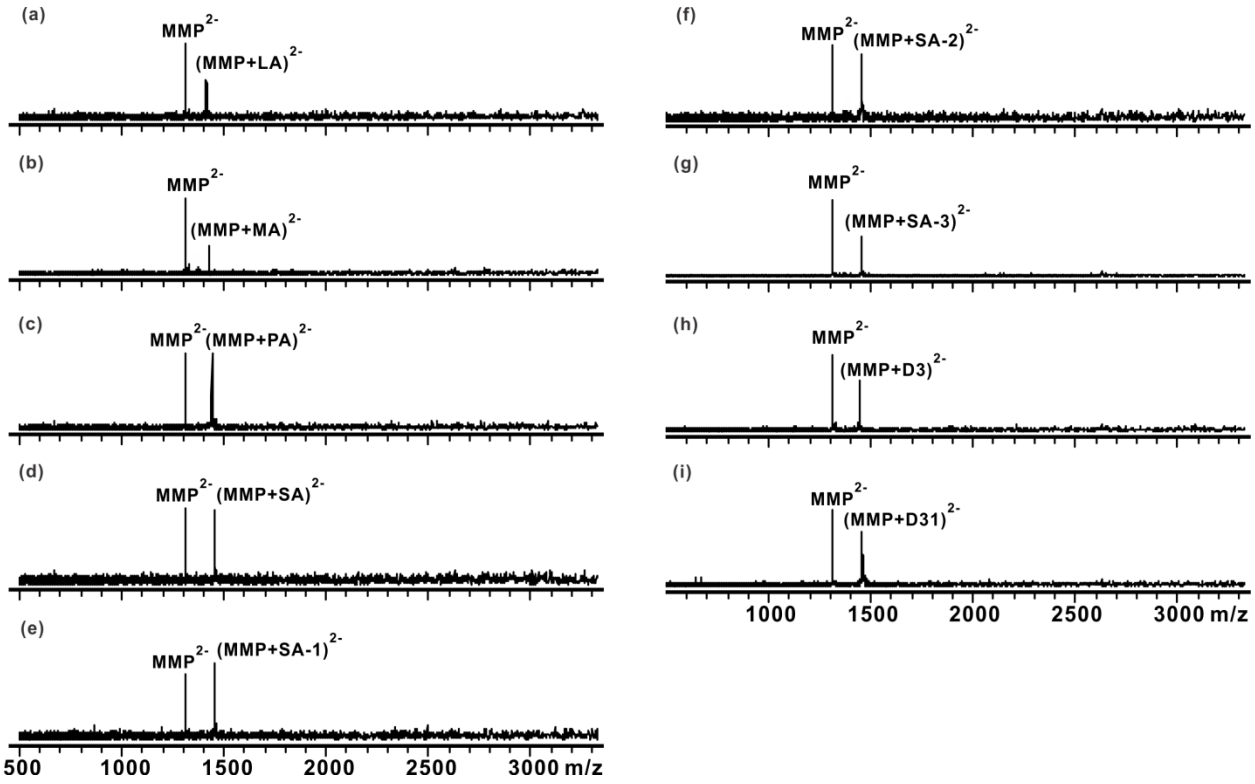

Figure S21. Illustrative BIRD mass spectra measured for (a) $(MMP + LA)^{2-}$ at a reaction temperature of 104 °C and a reaction time of 5 s; (b) $(MMP + MA)^{2-}$ at 119 °C and 3 s; (c) $(MMP + PA)^{2-}$ at 100 °C and 20 s; (d) $(MMP + SA)^{2-}$ at 100 °C and 40 s; (e) $(MMP + SA\text{-}1)^{2-}$ at 93 °C and 50 s; (f) $(MMP + SA\text{-}2)^{2-}$ at 95 °C and 40 s; (g) $(MMP + SA\text{-}3)^{2-}$ at 106 °C and 35 s; (h) $(MMP + D3)^{2-}$ at 100 °C and 20 s; and (i) $(MMP + D31)^{2-}$ at 100 °C and 20 s.

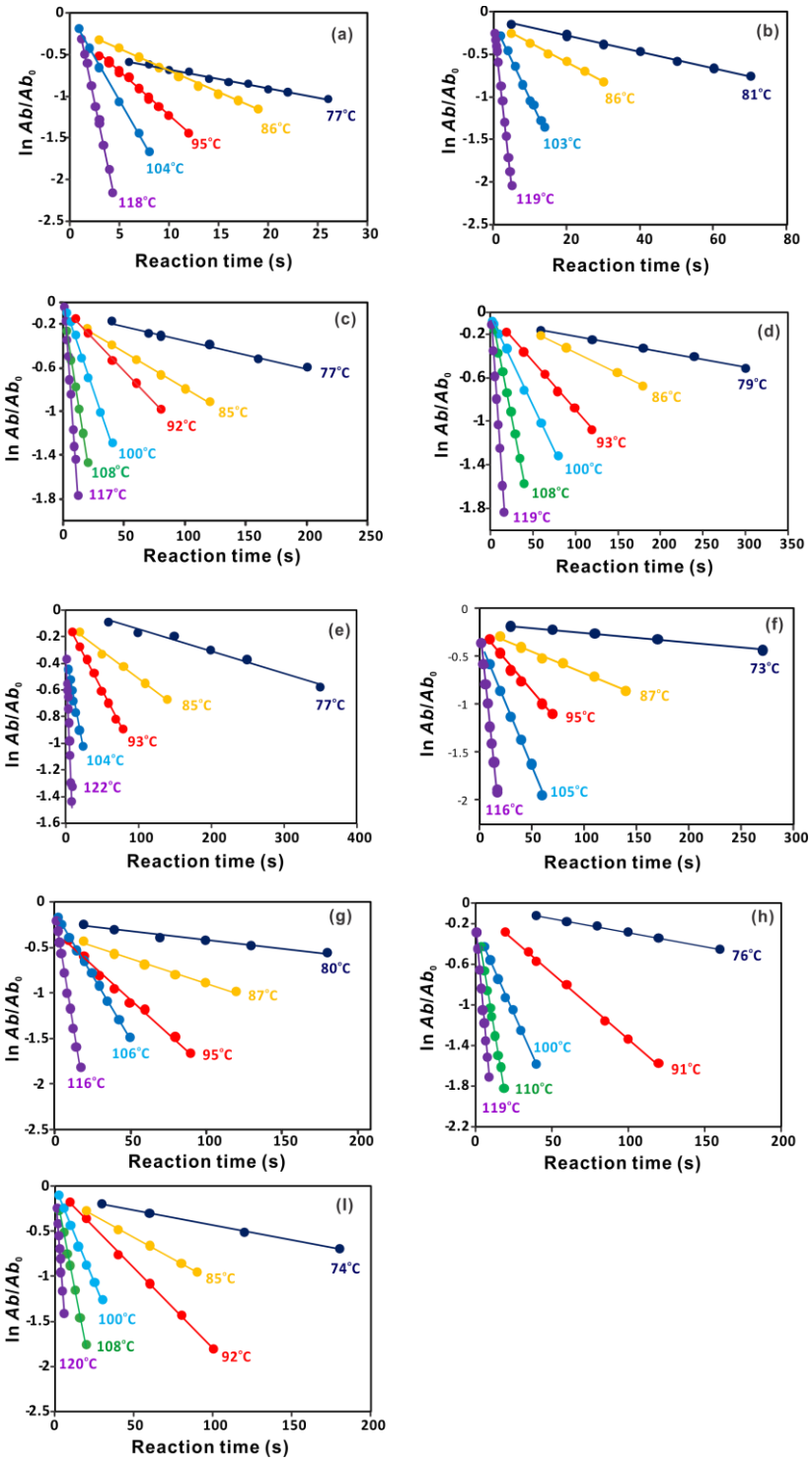

Figure S22. Plots of the natural logarithm of the normalized abundance (Ab/Ab_o) of (a) $(Lg + LA)^{7-}$, (b) $(Lg + MA)^{7-}$, (c) $(Lg + PA)^{7-}$, (d) $(Lg + SA)^{7-}$, (e) $(Lg + SA\text{-}1)^{7-}$, (f) $(Lg + SA\text{-}2)^{7-}$, (g) $(Lg + SA\text{-}3)^{7-}$, (h) $(Lg + PA\text{-}D3)^{7-}$ and (i) $(Lg + PA\text{-}D31)^{7-}$ ions versus reaction time at the temperatures indicated.

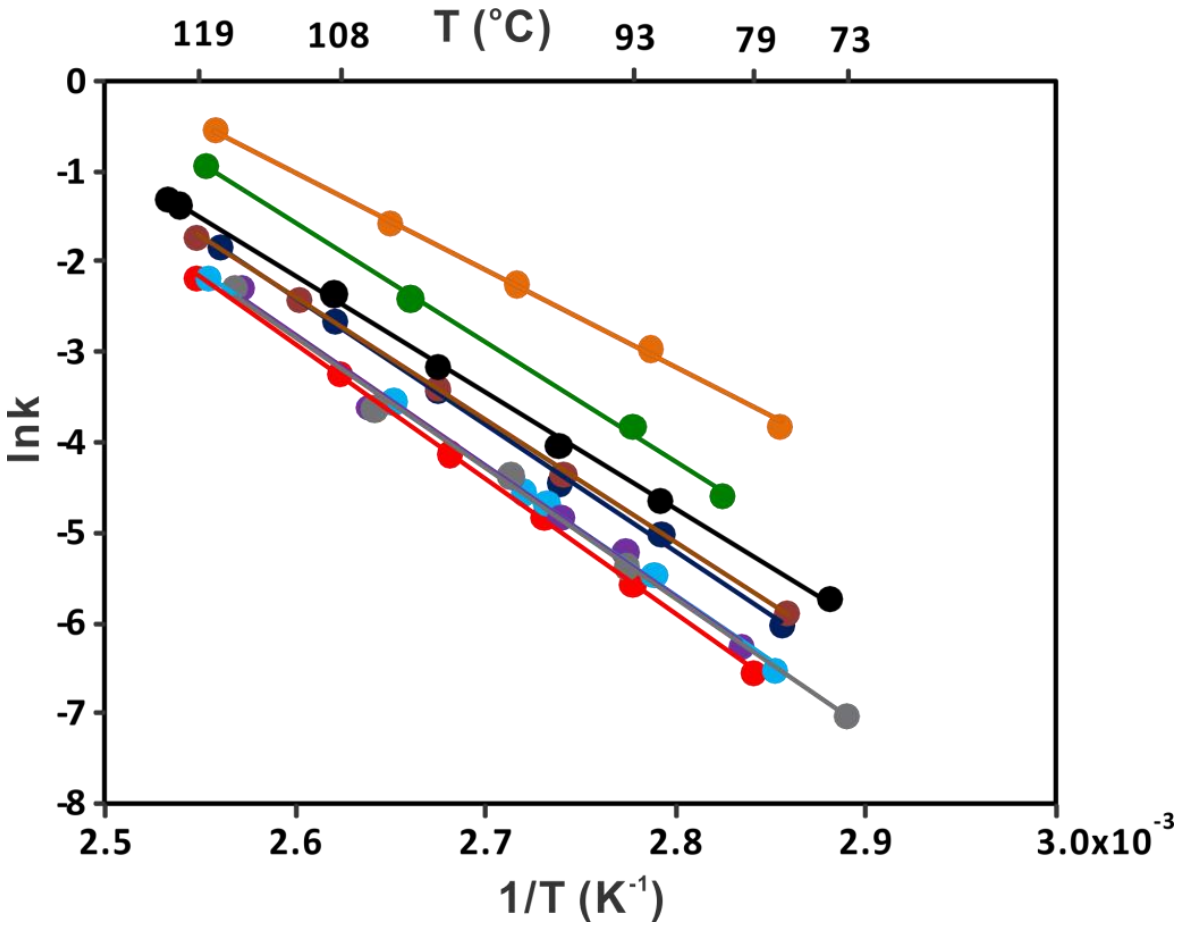

Figure S23. Arrhenius plots for the loss of neutral FA from the gaseous deprotonated (MMP + FA)$^{2-}$ ions, where FA = LA (●), MA (●), PA (●), SA (●),SA-1 (●), SA-2 (●), SA-3 (●),D3 (●),and D31 (●).

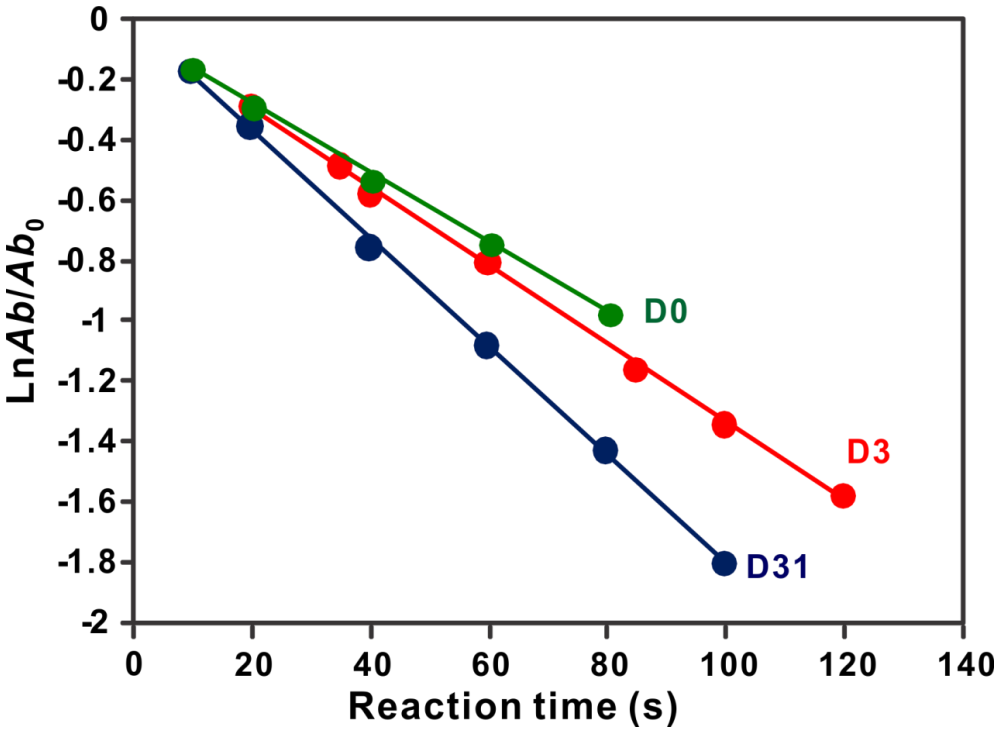

Figure S24. Plots of the natural logarithm of the normalized abundance (Ab/Ab_o) of (MMP + PA)$^{7-}$ ion versus reaction time measured at 92 °C for PA = D0 (•), (D3) (•), and (D31) (•).

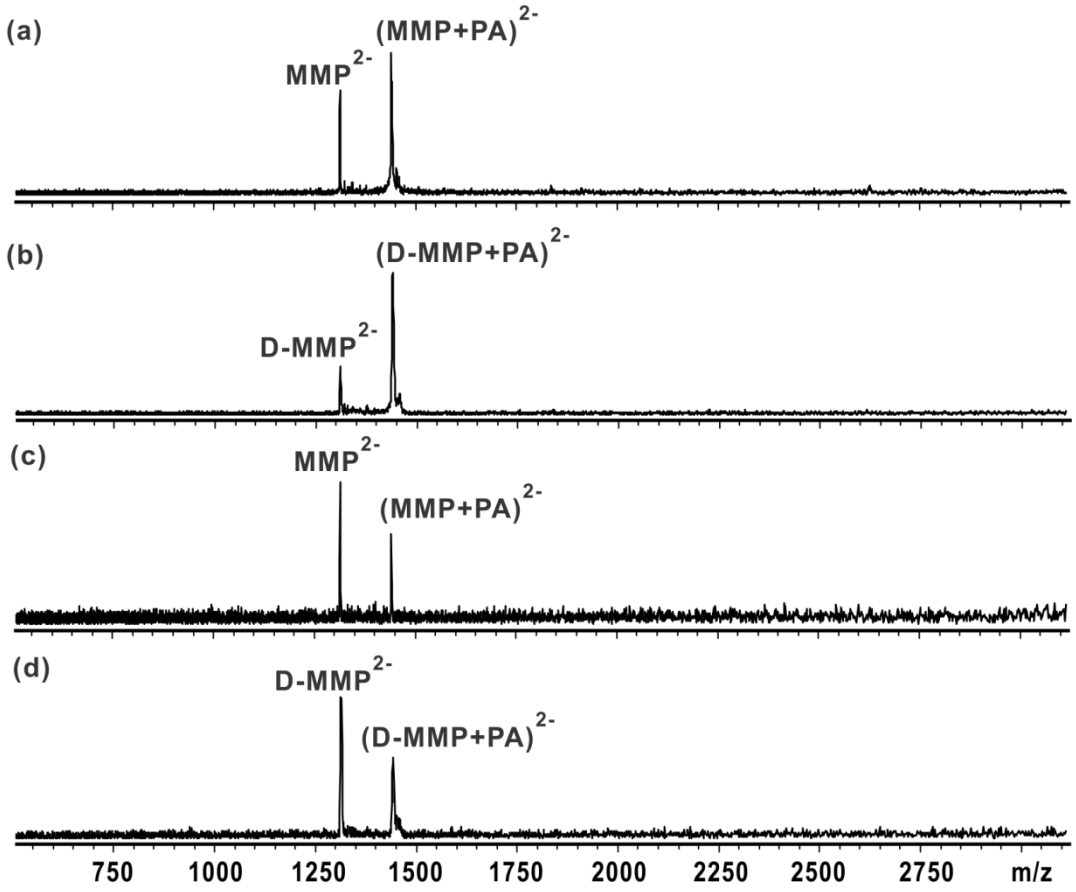

Figure S25. ESI mass spectra acquired for aqueous solutions (pH 8.5) of (a) MMP and PA, and (b) D-MMP and PA. Illustrative BIRD mass spectra measured for (c) $(MMP + PA)^{2-}$ at a reaction temperature of 117°C and a reaction time of 6 s, and (d) $(D\text{-}MMP + PA)^{2-}$ at a 117 °C, 6 s. Each solution contained 10 mM ammonium acetate and 10 mM imidazole.

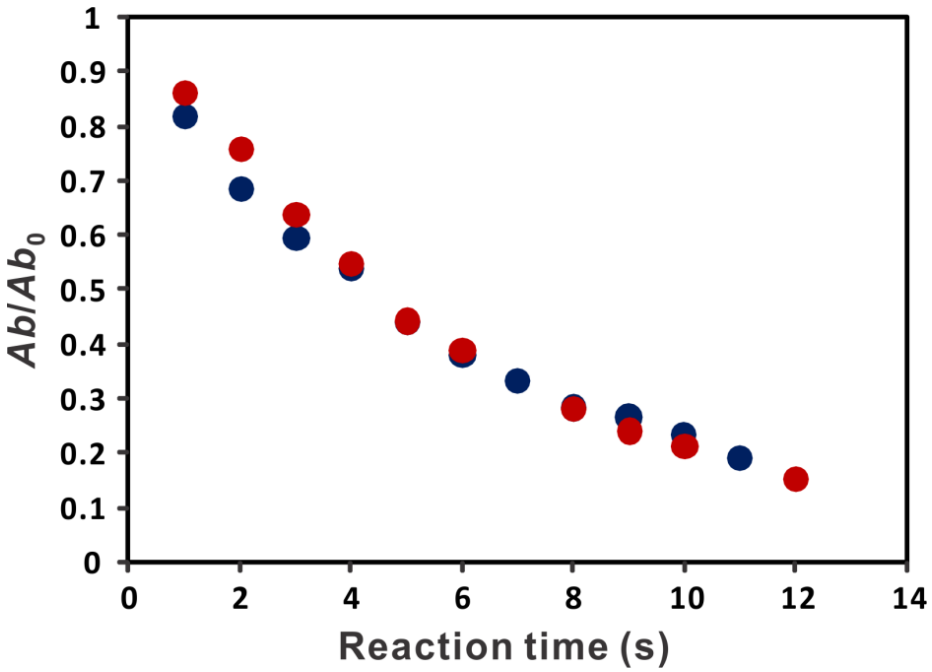

Figure S26. Plots of the normalized abundance (Ab/Ab_o) of $(MMP + PA)^{2-}$ (●) and $(D\text{-}MMP + PA)^{2-}$ (●) versus reaction time measured at 117 °C.

Table S4. Collision cross section (CCS) calibration. Charge states, m/z values, CCS values (from the literature[4-6]) and drift times (t_D) are listed for the calibrant ions: InsA, dT_{10} DNA, and PS. Also shown are the corrected drift times (t_D' and t_D'') and corrected CCS values (CCS').

charge state	m/z	literature CCS (Å^2)	drift time (t_D, ms)	corrected drift time (t_D', ms)	corrected CCS' (Å^2)	final corrected drift time (t_D'', ms)
InsA						
-2	1264.8	388	10.67	10.62	1020.92	1.68
-3	842.9	390	5.50	5.46	684.12	1.66
dT_{10} DNA						
-2	1488.3	447	11.88	11.82	1177.13	1.80
-3	991.9	446	6.82	6.78	783.00	1.90
-4	743.6	537	6.05	6.01	707.07	2.35
-5	594.7	627	5.17	5.13	660.46	2.66
-6	495.6	641	4.07	4.04	562.67	2.74
PS						
-1	505.2	163	8.25	8.22	839.60	0.73
-1	609.3	196	10.23	10.20	1014.12	0.83
-1	713.4	210	12.32	12.28	1090.05	0.93
-1	817.4	236	13.97	13.93	1227.96	1.01

-1	921.5	262	16.06	16.01	1365.79	1.10
-1	1025.5	276	18.04	17.99	1440.92	1.18

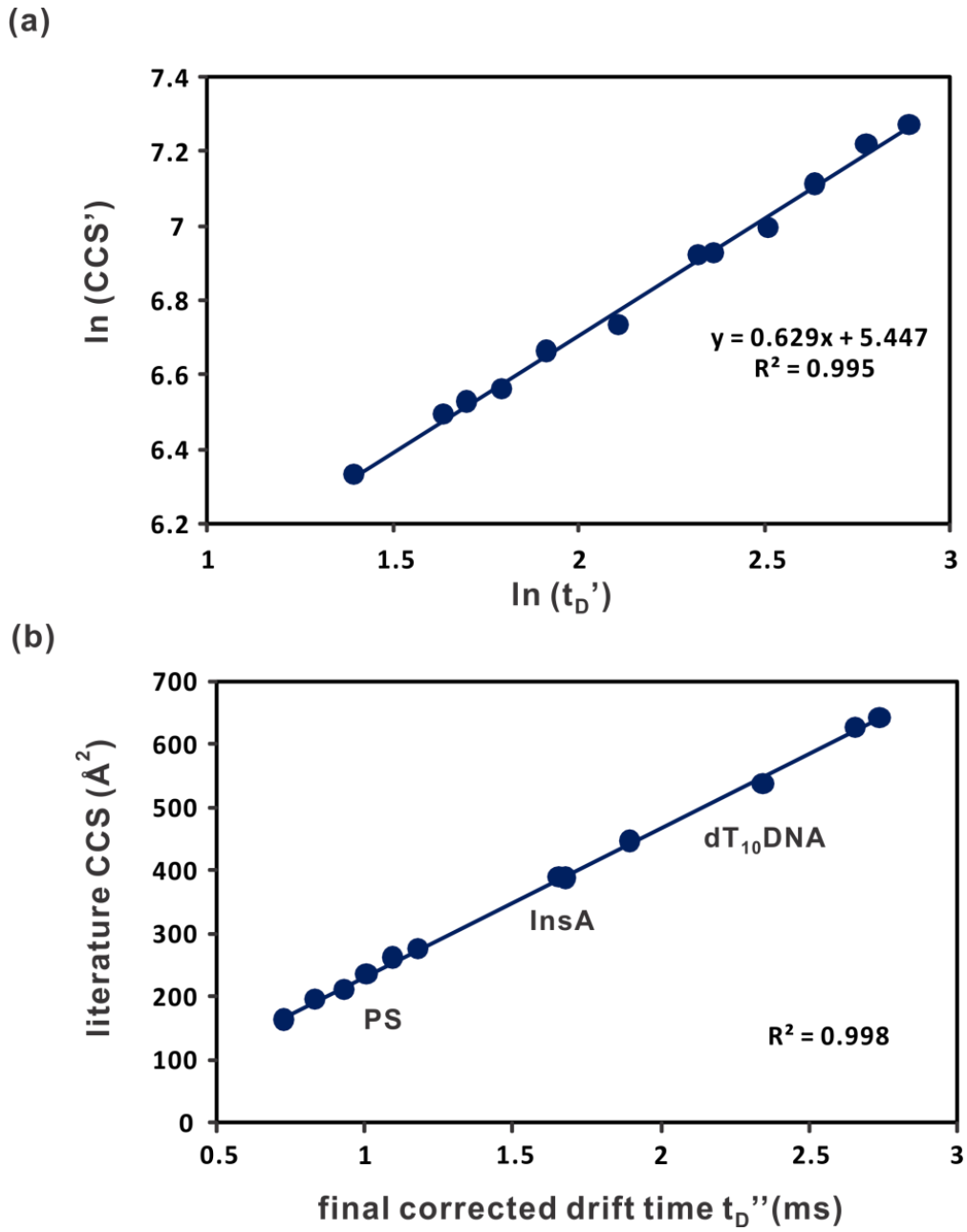

Figure S27. (a) Plot of ln(CCS′) versus ln(tD′) for the calibrants: InsA, dT10DNA, and PS. An exponential factor (X) of 0.629 was determined from the slope of the plot. (b) Calibration curve, based on the calibrants : InsA, dT10DNA, and PS, displayed as a linear plot of literature CCS values and final corrected drift times (tD″).

Table S5. Measured drift times (t_D), corrected drift times (t_D' and t_D") and collision cross sections (CCS) for deprotonated FA^-, MMP^{2-} and $(MMP + FA)^{2-}$ ions.

	m/z	drift time (t_D, ms)	corrected drift time (t_D', ms)	final corrected drift time (t_D'', ms)	Measured CCS (Å^2)
LA^-	199	5.55	5.53	0.59	136±4
MA^-	227	5.66	5.64	0.59	137±4
PA^-	255	5.88	5.86	0.60	139±4
SA^-	283	6.10	6.08	0.62	142±4
SA-1$^-$	281	5.77	5.75	0.60	137±4
SA-2$^-$	279	5.77	5.75	0.60	137±4
SA-3$^-$	277	5.77	5.75	0.60	137±4
MMP^{2-}	1310	11.66	11.61	1.78	414±8
$(MMP + LA)^{2-}$	1410	12.87	12.82	1.89	441±9
$(MMP + MA)^{2-}$	1424	13.20	13.15	1.92	448±9
$(MMP + PA)^{2-}$	1438	13.42	13.37	1.94	453±9
$(MMP + SA)^{2-}$	1452	13.64	13.59	1.96	457±10
$(MMP + SA\text{-}1)^{2-}$	1451	13.53	13.48	1.95	455±8
$(MMP + SA\text{-}2)^{2-}$	1450	13.53	13.48	1.95	455±10
$(MMP + SA\text{-}3)^{2-}$	1449	13.53	13.48	1.95	455±10

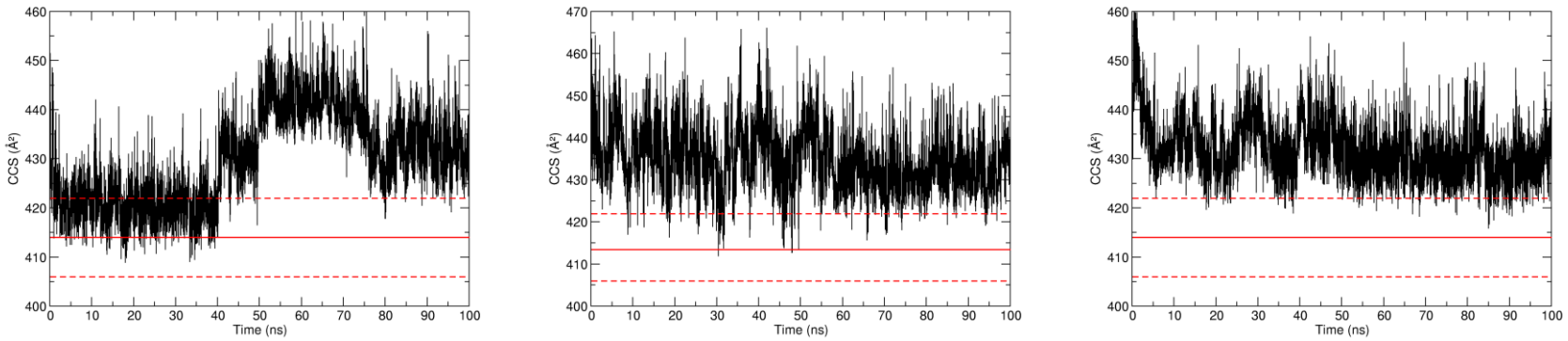

Figure S28. CCS for MMP^{2-} calculated over the 100 ns MD simulations. The red solid line indicates the experimental CCS value (**Table S4**) obtained from ion mobility measurements, and the red dashed lines indicate the uncertainty in the measured value.

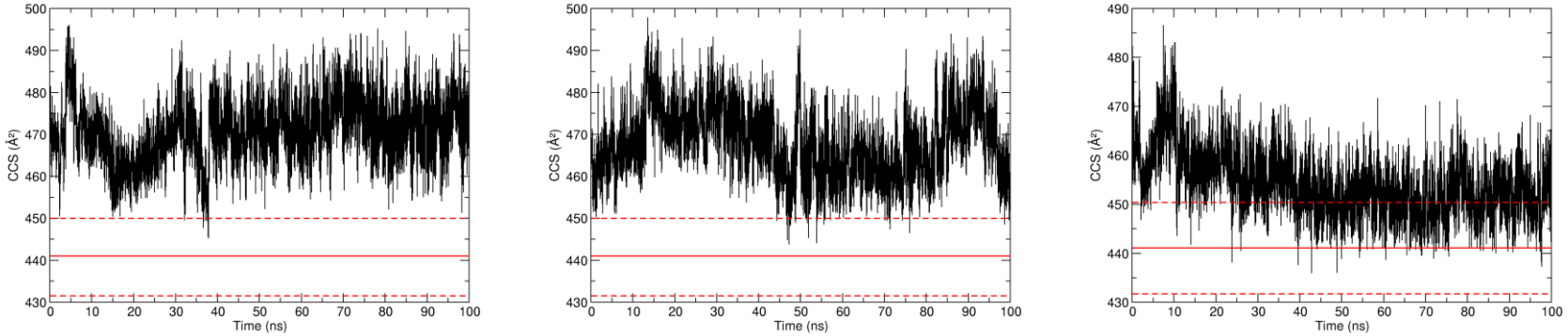

Figure S29. CCS for $(MMP^{2-} + LA)^{2-}$ calculated over the 100 ns MD simulations. The red solid line indicates the experimental CCS value (**Table S4**) obtained from ion mobility measurements, and the red dashed lines indicate the uncertainty in the measured value.

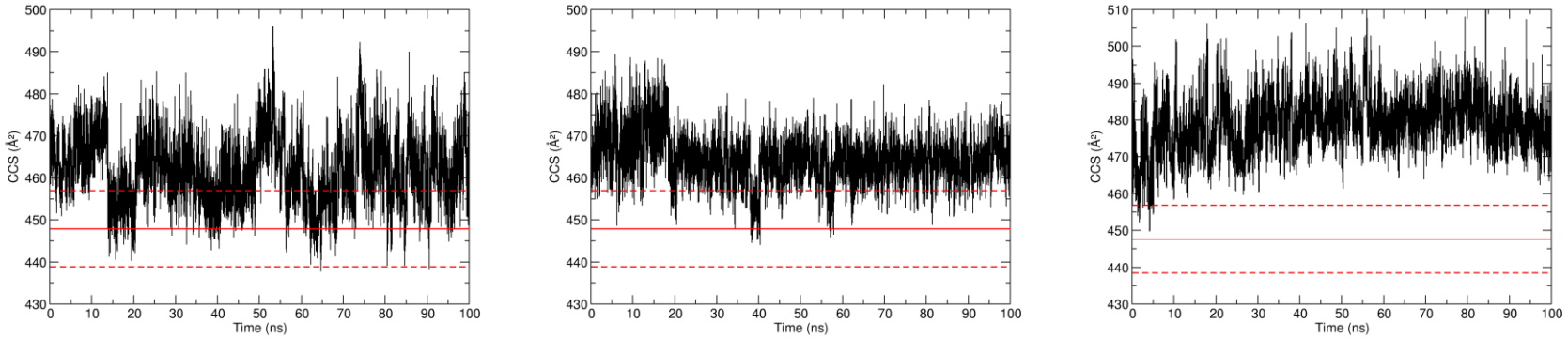

Figure S30. CCS for $(MMP^{2-} + MA)^{2-}$ calculated over the 100 ns MD simulations. The red solid line indicates the experimental CCS value (**Table S4**) obtained from ion mobility measurements, and the red dashed lines indicate the uncertainty in the measured value.

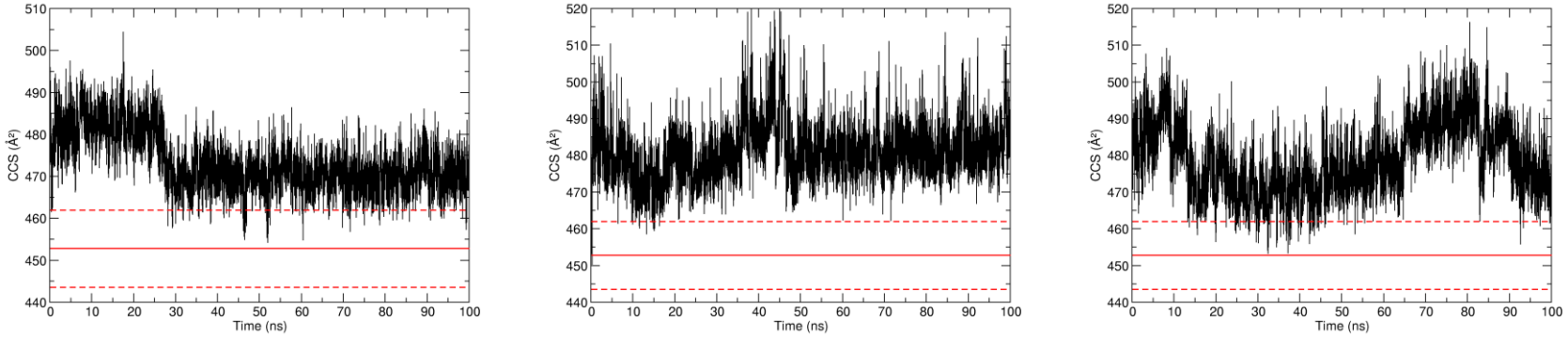

Figure S31. CCS for $(MMP^{2-} + PA)^{2-}$ calculated over the 100 ns MD simulations. The red solid line indicates the experimental CCS value (**Error! Reference source not found.**) obtained from ion mobility measurements, and the red dashed lines indicate the uncertainty in the measured value.

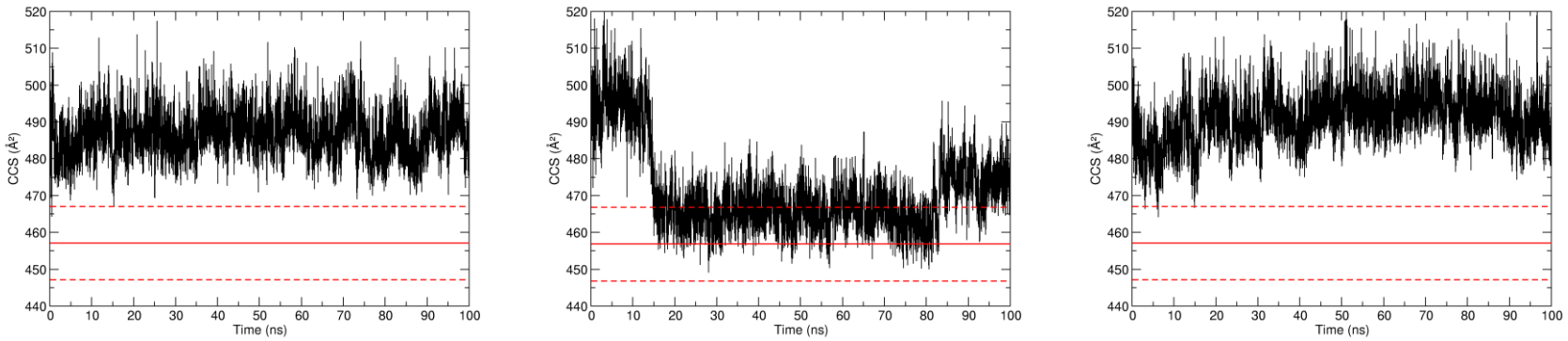

Figure S32. CCS for $(MMP^{2-} + SA)^{2-}$ calculated over the 100 ns MD simulations. The red solid line indicates the experimental CCS value (**Table S4**) obtained from ion mobility measurements, and the red dashed lines indicate the uncertainty in the measured value.

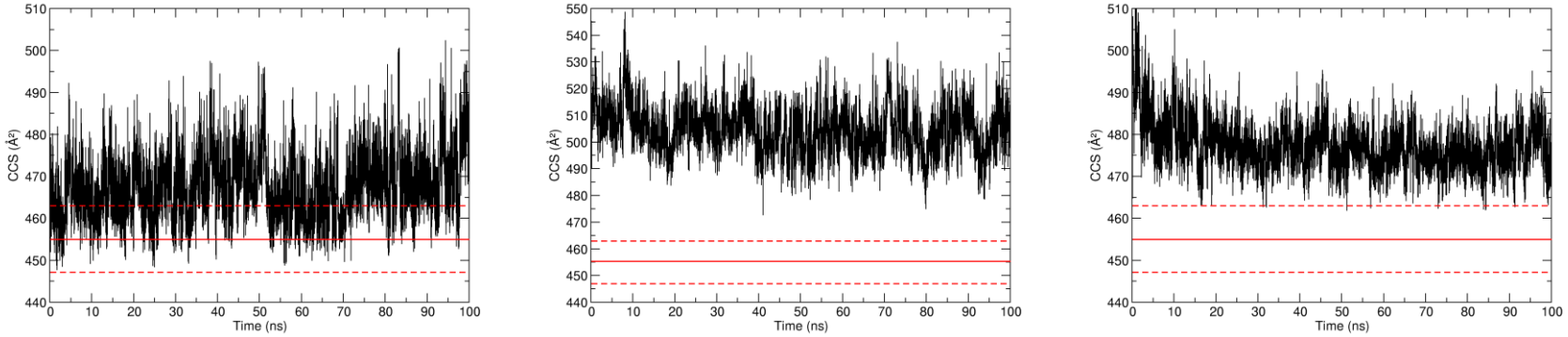

Figure S33. CCS for $(MMP^{2-} + SA\text{-}1)^{2-}$ calculated over the 100 ns MD simulations. The red solid line indicates the experimental CCS value (**Table S4**) obtained from ion mobility measurements, and the red dashed lines indicate the uncertainty in the measured value.

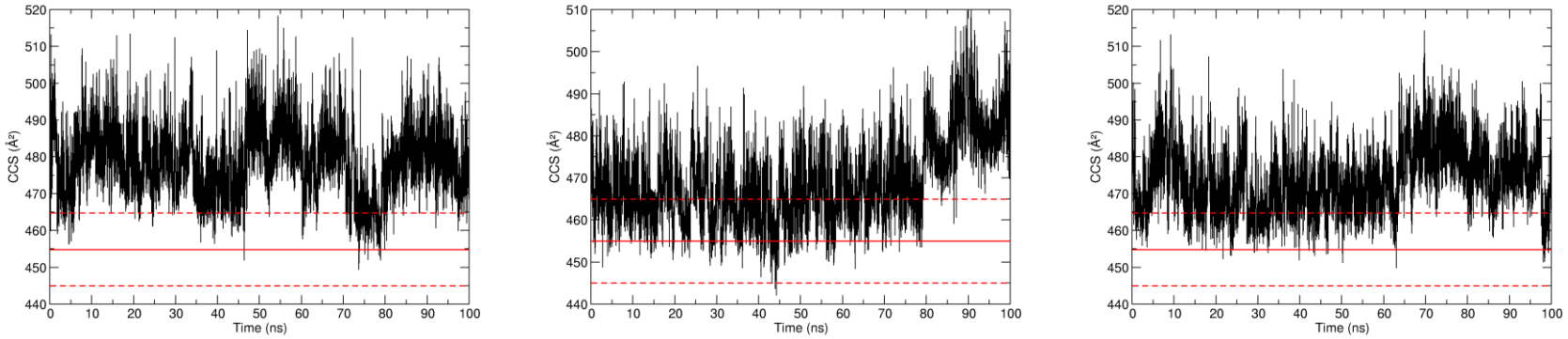

Figure S34. CCS for $(MMP^{2-}+SA\text{-}2)^{2-}$ calculated over the 100 ns MD simulations. The red solid line indicates the experimental CCS value (**Table S4**) obtained from ion mobility measurements, and the red dashed lines indicate the uncertainty in the measured value.

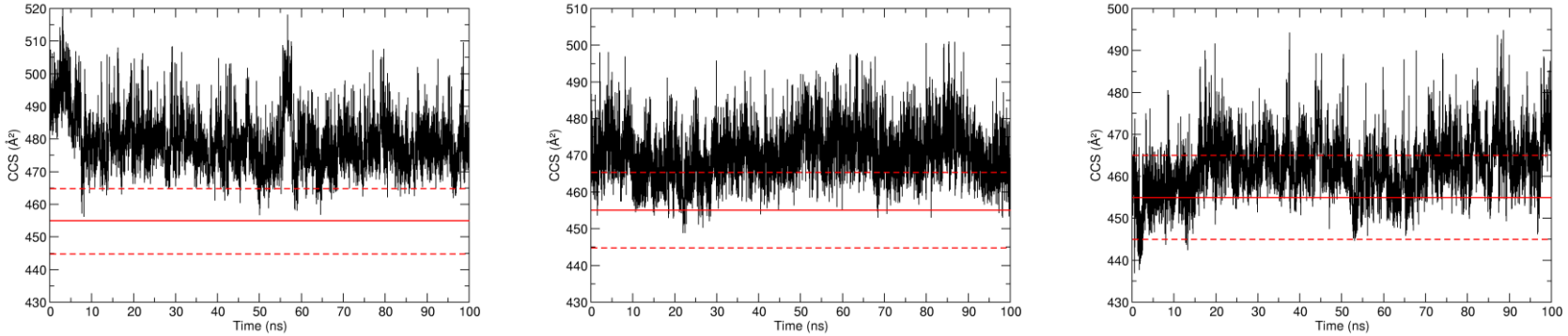

Figure S35. CCS for $(MMP^{2-} + SA\text{-}3)^{2-}$ calculated over the 100 ns MD simulations. The red solid line indicates the experimental CCS value (**Table S4**) obtained from ion mobility measurements, and the red dashed lines indicate the uncertainty in the measured value.

References:

[1] L. Liu, E. N. Kitova, J. S. Klassen, *J. Am. Soc. Mass Spectrom.* **2011**, *22*, 310–318.

[2] L. Liu, K. Michelsen, E. N. Kitova, P. D. Schnier, J. S. Klassen, *J. Am. Chem. Soc.* **2012**, *134*, 3054–3060.

[3] L. Liu, Y. Bai, N. Sun, L. Xia, T. L. Lowary, J. S. Klassen, *Chem. Eur. J.* **2012**, *18*, 12059–12067.

[4] T. Wyttenbach, G. von Helden, M. T. Bowers, *J. Am. Chem. Soc.* **1996**, *118*, 8355–8364.

[5] C. S. Hoaglund, Y. Liu, A. D. Ellington, M. Pagel, D. E. Clemmer, *J. Am. Chem. Soc.* **1997**, *119*, 9051–9052.

[6] J. V. Hamilton, J. B. Renaud, P. M. Mayer, *Rapid Comm. Mass Spectrom.* **2012**, *26*, 1591–1595.